Scilight

Earth Sciences Perspectives

https://www.sciltp.com/journals/esp



Review

Mars and Earth: Divergent Evolutionary Paths of Neighboring Worlds

Krutika Jangale [1], Kirtikumar Randive [1,*], Pratik Godbole [1], Kaustubh Deshpande [1], Tanushree Nikhure [1], Sanjeevani Jawadand [2], M. L. Dora [3] and M. Santosh [4,5,6]

[1] Department of Geology, RTM Nagpur University, Nagpur 440001, India
[2] Shri Mathuradas Mohota College of Science, Nagpur 440009, India
[3] School of Environmental Sciences, Jawaharlal Nehru University, New Delhi 110067, India
[4] China University of Geosciences Beijing, Beijing 10083, China
[5] Yonsei Frontier Lab, Yonsei University, Seoul, Republic of Korea
[6] Faculty of Science, Kochi University, Kochi 780-8520, Japan
* Correspondence: randive101@yahoo.co.in

How To Cite: Jangale, K.; Randive, K.; Godbole, P.; et al. Mars and Earth: Divergent Evolutionary Paths of Neighboring Worlds. *Earth Sciences Perspectives* **2026**, *1*(1), 3.

Received: 25 July 2026
Revised: 22 October 2026
Accepted: 30 October 2026
Published: 26 November 2026

Abstract: Mars shares striking superficial similarities with Earth, including its day length, axial tilt, and a history of liquid surface water. However, whether Mars represents a planetary twin, a distant cousin, or an entirely distinct system remains a central debate. This review synthesizes current knowledge on Martian geomorphology, atmospheric dynamics, volcanic and sedimentary records, mineralogical composition, and astrobiological potential using data from orbital missions, rovers, and meteorites. We demonstrate that fundamental differences in planetary dynamics, atmospheric stability, and magnetic shielding ultimately precluded long-term surface habitability on Mars. The absence of sustained plate tectonics, the lack of a global dipolar magnetosphere, and extreme climate variability driven by chaotic obliquity cycles steered Mars down a radically divergent evolutionary trajectory. Consequently, while Mars may have hosted transiently habitable environments, particularly in the subsurface, it is not a true analog to Earth. Instead, it represents a distinct planetary system with episodic habitability tightly constrained by unique geological and climatic drivers.

Keywords: martian geology; astrobiology; habitability; martian meteorites; martian surface

1. Introduction

Mars, the fourth planet from the Sun, is an important subject of comparative planetology among the terrestrial planets [1,2]. Its heliocentric distance varies from approximately 206.65 to 249.26 million kilometres. The planet's distinctive reddish appearance and geological features have attracted human interest since antiquity. In historical and popular accounts, Mars has often been described as Earth's "sibling" or "geological cousin," reflecting perceived similarities between the two planets and interest in their contrasting evolutionary histories. Advances in planetary science and robotic exploration have enabled increasingly detailed investigations of Mars, providing new opportunities to examine its geological, geophysical, and environmental evolution in comparison with Earth. A recent surge in orbital and surface missions has yielded high-resolution datasets that reveal a complex, geologically active world. This is evidenced by profound crustal magnetic anomalies, active modern sedimentation, cryospheric variability, and pervasive regolith development [3–8]. Central to these planetary investigations is the evaluation of Mars' past and present astrobiological potential [9]. While Mars exhibits striking physical symmetries to Earth, including nearly identical rotational periods and axial tilts, fundamental disparities in core dynamics, volatile inventories, and radiation shielding pose severe challenges to sustained surface

Copyright: © 2026 by the authors. This is an open access article under the terms and conditions of the Creative Commons Attribution (CC BY) license (https://creativecommons.org/licenses/by/4.0/).
Publisher's Note: Scilight stays neutral with regard to jurisdictional claims in published maps and institutional affiliations.

habitability. This review provides a valuable and well-organized synthesis of current understanding, offering a coherent comparative perspective on the geological controls on Martian habitability and their broader implications for understanding terrestrial planets. By systematically contrasting these drivers against terrestrial mechanisms, we critically evaluate whether Mars can be scientifically validated as Earth's planetary twin, an evolutionary cousin, or an entirely distinct class of terrestrial planetary system.

2. Martian Atmosphere

2.1. Chemical Composition of the Martian Atmosphere

The contemporary Martian atmosphere is hyper-attenuated, exhibiting a mean surface pressure of approximately 6.1 millibars and primarily consisting of carbon dioxide (CO_2; 95.32% by volume). The remaining volatile inventory comprises nitrogen (N_2; 2.7%), argon (Ar; 1.6%), and trace abundances of oxygen (O_2; 0.13%) and carbon monoxide (CO; 0.08%), alongside highly variable levels of water vapor (H_2O) and ozone (O_3) [10]. This gaseous mixture is largely transparent to incident visible light and soft ultraviolet (UV) radiation. However, it exhibits weak vibrational-rotational transitions in the near-infrared (NIR) spectrum (1–2 µm), restricting direct atmospheric absorption of incoming solar radiation to a meager 1% [11]. Conversely, CO_2 presents intense absorption bands in the thermal infrared (TIR) region, centered around 15 µm, 2.7 µm, and 4.3 µm (refer to Figure 1). These bands trap roughly 20% of upwelling surface-emitted thermal radiation, inducing a localized greenhouse effect. This radiative trapping is markedly inefficient compared to that of Earth's owing to the near-absence of complementary trace greenhouse gases, yielding a modern surface temperature elevation of only ~5 K [12,13].

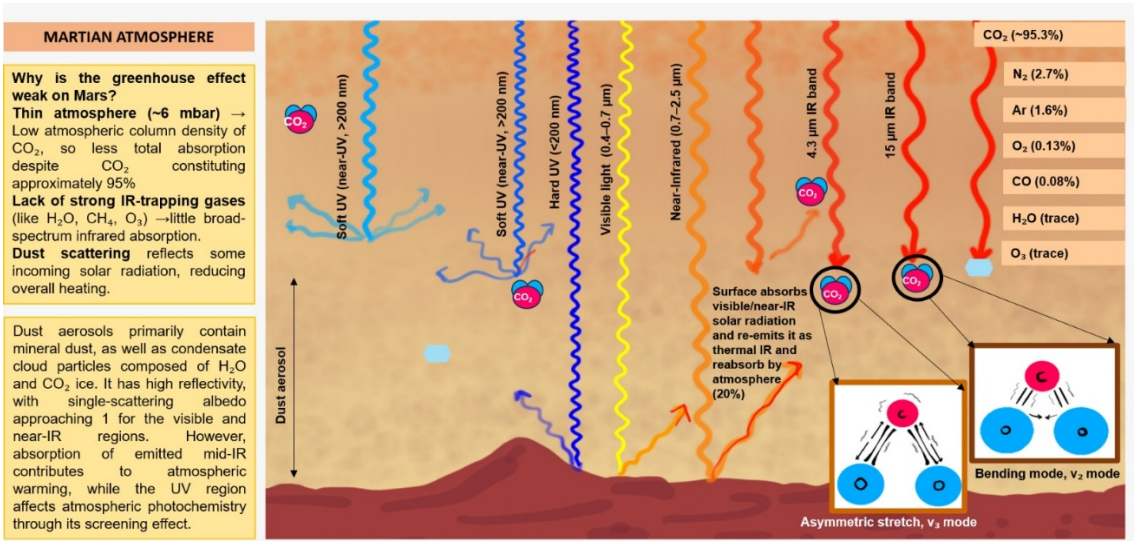

Figure 1. Martian atmospheric composition and its effect on solar radiation (modified after [10,11,13–16].

Beyond its gaseous composition, radiative transfer in the Martian atmosphere is heavily regulated by suspended particulate matter, including crystalline condensates (H_2O and CO_2 ices) and suspended mineral dust derived from long-term global rock weathering [14]. These aerosols dramatically alter the planet's spectral profile, climate forcing, and localized habitability [17]. Unlike Earth's moist atmosphere, Martian mineral dust exerts a pronounced screening effect that modulates the flux of surface-bound UV radiation, which alters atmospheric photochemistry, dictates surface sterilisation zones, and shields potential terrestrial bioburdens on landed hardware [15]. Paleoclimate models suggest this modern regime is a remnant of an ancient, denser atmosphere; early Martian surface pressures are estimated between 0.61 and 1.5 bars, meaning historical atmospheric masses were approximately 100–246 times the present-day value before long-term stripping and escape processes took effect [16].

Radiative-convective balances are further complicated by cloud microphysics. Water-ice clouds display a single-scattering albedo near 1 in the visible spectrum, meaning they strongly reflect sunlight while efficiently trapping upwelling thermal IR, leading to pronounced mid-altitude atmospheric heating zones [18]. In contrast, when ambient temperatures drop below the condensation threshold during polar nights, CO_2 ice clouds form spontaneously [19]. This process drives massive seasonal deposition in the form of macro-scale polar hood clouds and CO_2 snowfall [16,20]. This intense, cyclical exchange of volatiles between the atmosphere and the polar caps modulates the global mass distribution. The resulting seasonal mass asymmetry reshapes the planet's moment of inertia, inducing measurable fluctuations in Mars' rotational rate (length of day) and gravitational field profile.

Precision tracking of these transformations reveals seasonal peak-to-peak variations in the second (J_2) and third (J_3) zonal harmonics of approximately 6×10^{-9}, which equates to dynamic geoid fluctuations of 1.1 cm over a Martian year [21]. Integrating these geodetic variations remains essential for calibrating global atmospheric circulation models and modern surface-atmosphere transport simulations [22].

2.2. Effect of Planetary Dynamics on the Martian Atmosphere

Within the inner Solar System, Mars displays several striking geometric parallels to Earth, most notably an axial tilt (obliquity) of 25.19° and a solar day (sol) duration of 24 h and 39 min (a sidereal rotation period of 24.62 h). These orbital parameters dictate its diurnal and seasonal climate profiles. However, unlike Earth's ocean-buffered climate, the thermodynamic structure of the hyper-arid Martian atmosphere is rigidly governed by an instantaneous radiative-convective equilibrium between incident solar insolation and upwelling thermal infrared emissions from the surface. This radiative state is modulated by atmospheric momentum, sensible heat transport, and macro-scale circulation regimes driven by stark latitudinal thermal gradients.

Global atmospheric circulation on Mars is characterized by a pronounced, cross-equatorial Hadley overturning cell at low latitudes, supplemented by transient baroclinic cyclonic and anticyclonic wave systems within the winter extratropical wave-guides [14]. This atmospheric buoyancy is driven by differential solar forcing across highly variable surface albedos. Vertical and horizontal profiles captured by the Mars Climate Sounder (MCS) aboard NASA's Mars Reconnaissance Orbiter demonstrate intense zonal thermal variations with respect to both latitude and altitude [23]. A distinguishing feature of the modern Martian troposphere is that temperature decreases monotonically with altitude across most latitudes without a stabilizing, ozone-driven stratosphere like Earth's. During solstitial regimes, top-of-atmosphere solar forcing drives maximum temperatures directly over the summer poles while the winter poles remain plunged in hyper-cold polar nights; conversely, equinoctial phases exhibit symmetrical cooling from the equator outward toward both poles [14].

A fundamental divergence between the two worlds lies in their long-term orbital configurations. While Earth's obliquity is gravitationally stabilized by the Moon, oscillating narrowly between 22.1° and 24.5° over a stable 41,000-year cycle, Mars experiences massive, chaotic variations in obliquity ranging from 0° to nearly 60° (and theoretically up to 80°) over millions of years. This instability arises from the absence of a massive stabilizing natural satellite and strong gravitational perturbations from Jupiter acting on a highly eccentric orbit ($e \approx 0.093$). While Mars' current obliquity mirrors Earth's, driving familiar seasonal cycles, past deviations have triggered extreme climate states. At low obliquity (≤15°), global atmospheric collapse occurs as the bulk of the CO_2 atmosphere freezes directly onto the poles, dropping surface pressures to less than a millibar. Conversely, when obliquity exceeds 30° to 45°, a recurring state over the past 4 billion years, the poles receive greater annual insolation than the equator [7,24,25]. This high-obliquity forcing drives massive sublimation of polar volatiles, thickening the atmosphere, raising global surface pressures, and temporarily opening narrow microclimatic windows for transient liquid water stability before shifts in planetary orientation return Mars to its contemporary hyper-arid, frozen baseline [7] (Refer to Figure 2).

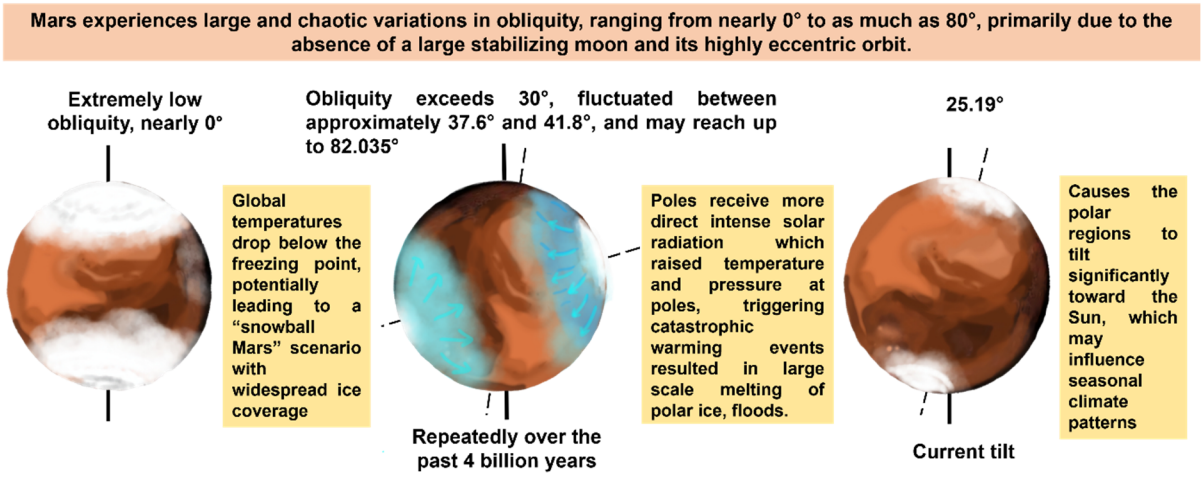

Figure 2. Martian chaotic obliquity and its results (modified after [7]).

2.3. Martian Dust Devils and Wind Patterns

Dust devils are micro-scale, vertically aligned convective vortices that develop within the planetary boundary layer due to intense local solar heating. On Mars, these rotating columns of air lift fine-grained particles directly into atmospheric suspension. They serve as a primary mechanism driving the planet's baseline atmospheric dust opacity, particularly during aphelion when solar forcing is weaker yet remains thermodynamically sufficient to initiate localized convection [26,27]. These phenomena hold critical engineering significance, as they alter solar array efficiency, degrade optical instruments, and dictate localized wind shear profiles relevant to low-altitude aerial exploration platforms like the Ingenuity helicopter.

In-situ datasets from the Perseverance rover demonstrate that dust devils are exceptionally frequent within Jezero Crater, where strong thermal contrasts arise from heterogeneous surface albedos [28]. Unregulated solar radiation rapidly heats the low-density near-surface atmosphere, causing parcel buoyancy and inducing vortex rotation via the conservation of angular momentum [26]. These vortices typically stabilize along the margins of open convection cells where ascending thermal plumes generate highly localized low-pressure cores. The resulting pressure deficit draws in high-pressure ambient air, sustaining cyclonic winds that peak during diurnal insolation maxima across arid, barren landscapes [29,30].

The intense shear stress concentrated within the vortex walls overcomes particle threshold friction velocities, lifting dust via saltation and direct suspension [31]. This localized mass transport shapes regional aeolian landforms and modulates global radiative balances. Orbital tracking reveals that these vortices leave distinct tracks across the terrain; these paths frequently exhibit higher reflectivity over time as the core winds strip away dark, fine-grained dust to expose brighter underlying substrates [26]. Morphologically, Martian dust devils manifest as inverted cones with narrow surface apices that expand into broad, columnar geometries at higher planetary boundary layer altitudes [32]. Boundary conditions influence their physical structures: rugged, obstacle-strewn alluvial terrains promote irregular V-shaped profiles, whereas smooth, uniform surfaces like Martian playas yield symmetric, highly stable columns.

Beyond planetary weather dynamics, these convective vortices drive aggressive mechanical erosion across the landscape. The entrained dust comprises crystalline or amorphous mineral phases that actively abrade geological structures and exposed spacecraft materials via high-velocity sandblasting. Recent experimental wear testing demonstrates that Martian dust simulants are highly abrasive, causing up to 1.5 times more solid particle erosion by mass at oblique impact angles compared to terrestrial dust equivalents [33]. This abrasion converts particle kinetic energy into localized thermal and mechanical stress, triggering micro-fracturing and accelerating structural deformation depending on the properties of the target alloy [33]. Consequently, resolving the precise dynamics of surface dust lifting and convective transport remains paramount for refining global Martian climate simulations and predicting the operational lifespans of prospective surface missions [34].

3. Martian Magnetosphere and Magnetic Field

A planetary magnetosphere is the spatial region surrounding a celestial body dominated by its intrinsic magnetic field, typically sustained by the convective motion of conductive fluid within its core via a magnetohydrodynamic dynamo. While Earth possesses a robust, geodynamo-driven dipolar magnetosphere that shields its atmosphere from the solar wind and galactic cosmic rays, contemporary Mars lacks a global intrinsic magnetic field [35]. Because of Mars' smaller planetary mass, its thermal evolution progressed rapidly, leading to early core cooling that drastically altered its internal dynamics. This rapid heat loss presumably quenched the thermal convection necessary to sustain an active core dynamo early in Martian history [36]. Magnetometer data from the Mars Global Surveyor (MGS) revealed that instead of a global dipole, Mars exhibits localized crustal remanent magnetic fields. The strongest of these localized anomalies peak at approximately 1500 nanotesla, which is over 40 times weaker than Earth's typical surface field. These crustal fields are intensely asymmetric; they are virtually absent across the younger northern lowlands but remain profoundly preserved across the ancient, heavily cratered southern highlands, deep impact basins, and portions of the Tharsis volcanic province [4].

Interestingly, the modeled paleomagnetic polarities indicate a complete inversion relative to modern terrestrial conventions, with ancient magnetic north corresponding to the southern hemisphere [37,38]. This complex magnetic spatial structure has been illuminated by recent geophysical missions. Seismic data from NASA's In-Sight lander confirmed that Mars possesses a solid, crystalline inner core surrounded by a liquid outer core. However, recent revisions to these seismic models demonstrate that this core is enveloped by a distinct, highly insulating basal layer of molten silicates (~150 km thick) at the base of the mantle [39]. This molten silicate blanket acts as a thermal insulator, trapping core heat and suppressing the core-mantle boundary heat flux. The resulting reduction in core thermal convection, combined with the potential absence of a solid inner core to drive compositional convection, explains why a global dynamo cannot be sustained today despite the core remaining entirely liquid [40,41].

Magnetometer (MAG) and Electron Reflectometer (ER) datasets from MGS confirmed that these localized crustal magnetic signatures vary dynamically across the surface, recording a complex timeline of planetary evolution [38]. On Earth, directional shifts in the magnetic field are preserved via paleomagnetism, wherein iron-bearing minerals like magnetite align with ambient field lines as basaltic lavas cool past their Curie temperatures [42]. Because direct oriented rock samples are currently unavailable from the Martian surface, Arkani-Hamed and Boutin, (2004) bypassed this limitation by modeling isolated magnetic anomalies using multi-altitude MGS data. Their inversions revealed distinct clusters of paleopoles that deviate drastically from the planet's modern rotational axis. This geometric mismatch provides compelling evidence that Mars underwent substantial true polar wander (TPW) shifting its rotational axis relative to its crust alongside multiple magnetic field reversals before the global dynamo completely shut down [42].

Due to the lack of a protective global dipole, the solar wind collides directly with the upper Martian atmosphere. This unhindered solar wind interaction generates an induced magnetosphere through magnetic pileup and ionospheric mass-loading [43]. Interplanetary magnetic field (IMF) lines carried by the solar wind drape around the planet, creating a structured magneto-plasma envelope. *In-situ* plasma and magnetic field instrumentation aboard NASA's MAVEN spacecraft confirmed that this interaction creates a permanent layer of magnetized plasma along the dayside ionopause (refer to Figure 3). This induced barrier continuously scavenges planetary ions, channeling them along draped magnetic field lines from the dayside atmospheric reservoir into the magnetotail, driving the long-term volatile stripping that fundamentally transformed Mars from a wet, transiently habitable world into a frozen desert [44].

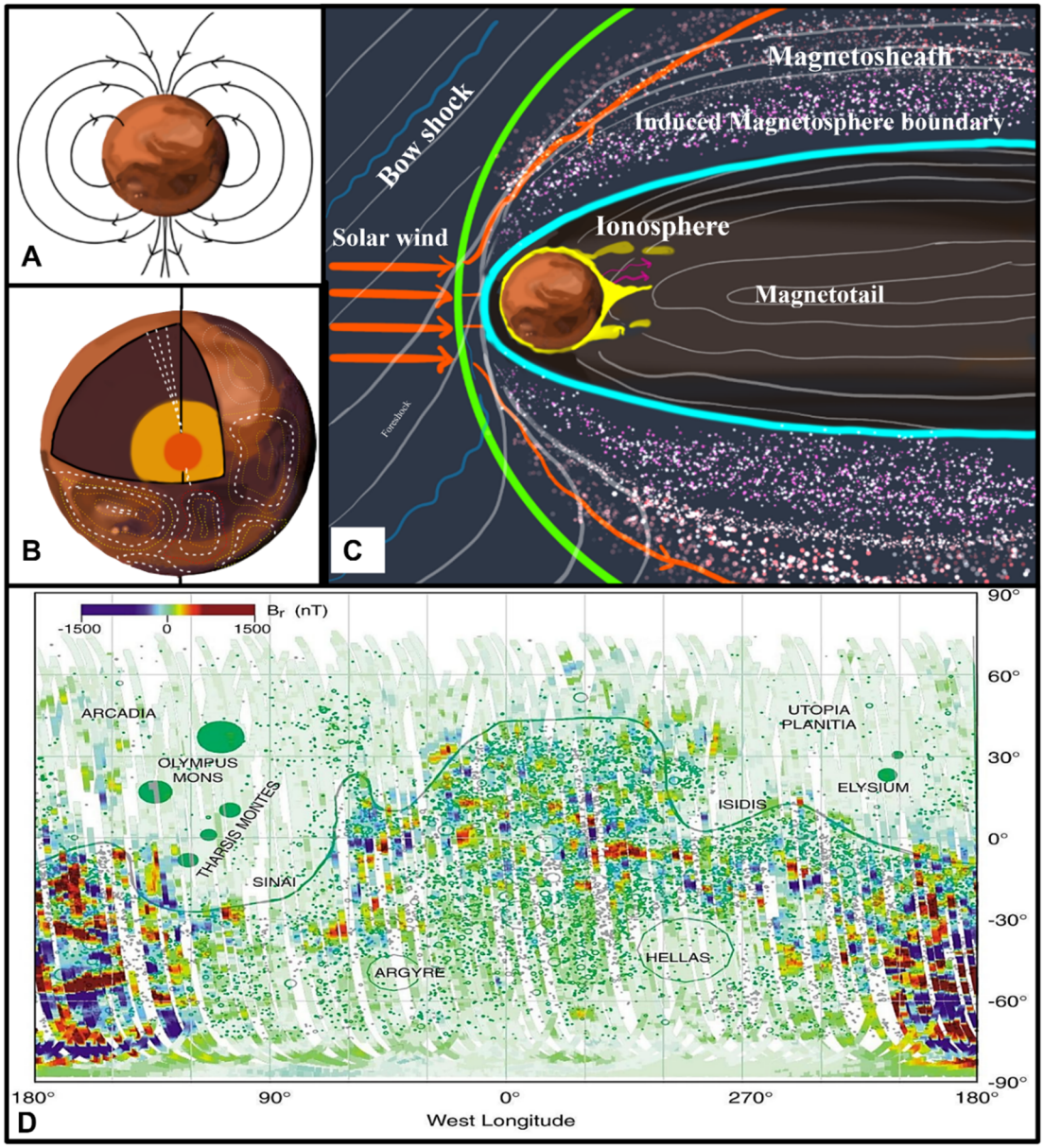

Figure 3. (**A**) Early Martan magnetic field before ~4 Ga, (**B**) Current Crustal remanent magnetization, (**C**) Induced Magnetosphere due to interaction of the ionosphere and the solar winds, (**D**) Map of Mars showing the intensity of

crustal magnetic fields as measured and color-coded by NASA's Mars Global Surveyor, Dark green markers indicate major volcanoes and large impact craters. Light green lines show spacecraft tracks below 200 km altitude. The solid line marks the Martian crustal dichotomy boundary separating the northern lowlands and southern highlands (modified after Source: NASA/JPL/GSFCNASA/JPL/GSFC, 1999) [44,45].

4. Martian Meteorites

Meteorites serve as pristine geochemical time capsules that afford direct insights into the magmatic, atmospheric, and chronological evolution of Mars. By evaluating the isotopic, elemental, and mineralogical inventories of these samples, researchers can model mantle differentiation timescales, planetary cooling profiles, and ancient volatile reservoirs. To date, over 300 distinct specimens have been officially recognized as Martian in origin [6]. The overwhelming majority of these samples are mafic to ultramafic igneous rocks that encapsulate pristine samples of the ambient Martian atmosphere within shock-melted glass phases. Furthermore, these meteorites preserve delicate records of post-crystallization processes, including low-temperature aqueous alteration features [46], evaporitic salt deposits [47], and complex impact-generated shock melt pockets encapsulating local regolith components [48].

The vast majority of Martian meteorites belong to the co-genetic SNC (Shergottite-Nakhlite-Chassignite) group. This planetary linkage was definitively confirmed when isotopic analyses of noble gases trapped inside the shock-melted phases of the shergottite EETA79001 yielded a flawless elemental match to the ambient Martian atmospheric composition measured *in-situ* by the Viking landers [49,50]. While these fine-grained igneous rocks crystallized at distinct intervals throughout Martian history, cosmic-ray exposure (CRE) age models indicate they were excavated and launched into space by highly energetic, localized impact events within the last 1 to 20 million years. Chronologically, the SNC suites span billions of years: while the majority of shergottites and nakhlites record relatively youthful igneous activity (~150 Ma to 1.3 Ga), the anomalous orthopyroxenite ALH 84001 yields a deep lutetium-hafnium (Lu-Hf) crystallization age of 4091 ± 30 million years, validating it as a direct sample of the ancient, heavily cratered Martian crust [51].

4.1. Shergottites

Shergottites represent the most abundant class of Martian meteorites, believed to have crystallized from basaltic and ultramafic parent melts generated via partial melting of a depleted Martian mantle. These rocks predominantly formed within expansive surface lava flows or shallow sub-surface intrusions rather than within deep, plume-driven volcanic plumbing systems [52,53]. They are classified into three distinct lithological subgroups:

(1) Basaltic Shergottites**:** Comprising volcanic specimens composed of roughly equal modal abundances of pyroxene (clinopyroxenes augite and pigeonite) and plagioclase, typically supplemented by trace microcrystalline mesostasis. They are distinctly olivine-free. The presence of accessory baddeleyite (ZrO_2) enables high-precision uranium-lead (U-Pb) dating. These samples bear acute structural indicators of extreme shock metamorphism, most notably the widespread solid-state transformation of plagioclase into isotropic maskelynite glass (e.g., Shergotty, Zagami, EETA 79001B, QUE 94201, Los Angeles, NWA 480, Dhofar 378).

(2) Lherzolitic (Poikilitic) Shergottites**:** Plutonic variants exhibiting a strong cumulate texture characterized by coarse olivine and chromite crystals enclosed within macrocrystic orthopyroxene oikocrysts. Minor phases include intercumulus maskelynite, iron-titanium oxides, sulfides, and phosphates. These rocks record intense high-pressure shock metamorphism ranging between 30 and 45 GPa, evidenced by the distinct brown staining of olivine due to impact-induced Fe^{3+} oxidation (e.g., ALH 77005, LEW 88516, Y793605, GRV 020090, NWA 1950).

(3) Olivine-Phyric Shergottites**:** Characterized by large, highly magnesian olivine phenocrysts set within a fine-grained basaltic groundmass. These specimens represent primitive, mantle-derived magmas that underwent minimal crustal assimilation during ascent (e.g., NWA 2046, NWA 4925) [54,55].

4.2. Nakhlites

Initially recovered following the historic 1911 El Nakhla falls in Egypt, nakhlites are clinopyroxenites rich in calcic augite, accompanied by minor orthopyroxene, fayalitic olivine (9–17%), and an absolute interstitial mesostasis fraction of 8–20% [56]. Certain specimens (e.g., Y000593, MIL 03346) display prominent accessory iron-titanium oxides. A defining feature of the nakhlite suite is the preservation of pre-terrestrial, hydrous alteration veins filled with iddingsite, a complex mixture of clay minerals, iron oxides, and ferrihydrites. These veins provide unambiguous structural proof that their host igneous provinces interacted with liquid, solute-rich surface or sub-

surface water approximately 620 million years ago [57]. Geochemically, nakhlites are strongly enriched in calcium and light rare earth elements (LREEs) but are severely depleted in aluminum, indicating accumulation within thick, stagnant lava flows or shallow sills within the major volcanic provinces of Tharsis, Elysium, or Syrtis Major (e.g., Nakhla, Lafayette, Governador Valadares, NWA 817, MIL 03346).

4.3. Chassignites

Chassignites are extremely rare Martian dunitic cumulates composed almost exclusively of cumulus olivine (~90%), with minor contributions from clinopyroxene (3–5%), plagioclase/maskelynite (2%), and accessory chromite (2–5%) [58]. The type specimens, Chassigny and NWA 2737, display distinct compositional variability; the olivine in NWA 2737 is notably more forsteritic (Fo_{79}) than the iron-rich variety found in Chassigny (Fo_{69}). Melt inclusions within these minerals preserve hydrous amphiboles and kaersutite, indicating crystallization within an uncommonly volatile-rich, oxidizing magmatic environment [59]. Structurally, these rocks exhibit an intense shock-induced smoky brown discoloration caused by the dispersion of nanometer-scale metallic iron particles throughout the shocked olivine crystal lattices. Crystallization models demonstrate that while NWA 2737 records a youthful magmatic age of 160–190 Ma, Chassigny reflects an older ~1.3 Ga event matching the nakhlite emplacement timeline [60] (Refer to Table 1).

Table 1. End-member mineral compositions and major element geochemistry of standard Martian meteorite suites (adapted from [54,55,61]).

Meteorite Class	Olivine Component (Mol% Fo)	Pyroxene Component (Mol% En)	Clinopyroxene Specie & Abundance (CaO wt%)	Plagioclase/Maskelynite (Mol% An)
Shergottites	$Fo_{66–78}$	$En_{32–77}$	Augite (10–22 wt%) Pigeonite (6–12 wt%)	$An_{39–70}$
Nakhlites	$Fo_{15–42}$	$En_{37–62}$	Augite (12–16 wt%) Pigeonite (Rare)	$An_{23–40}$
Chassignites	$Fo_{68–80}$	$En_{49–56}$	Minor Augite (10–14 wt%) Pigeonite (Absent)	$An_{30–80}$
ALH 84001 (Orthopyroxenite)	$Fo_{65–70}$ (Trace)	$En_{68–72}$ (Dominant)	Augite (2–4 wt%) Pigeonite (Absent)	$An_{30–35}$ (Interstitially Shocked)

4.4. ALH 84001

Collected from the Allan Hills icefield in Antarctica, ALH 84001 is the sole known Martian orthopyroxenite, consisting of roughly 96% orthopyroxene, 2% chromite, 1% maskelynite, and 0.15% phosphates [60]. This specimen stands apart from the standard SNC suites due to its ancient Noachian crystallization age (4.09 to 4.12 Ga), rendering it a definitive relic of the primordial Martian crust. Beyond its antiquity, ALH 84001 remains a cornerstone of astrobiological literature due to the presence of secondary polycyclic aromatic hydrocarbons (PAHs) associated with complex carbonate globules [62]. These carbonate features preserve a unique bi-mineralic assembly of fine-grained magnetite and iron sulfides alongside periclase and hematite, recording the dynamic chemical, thermal, and potentially biogenic milestones of early Mars.

5. Martian Rock Types

5.1. Martian Crust

In-situ chemical analyses and global orbital spectroscopy demonstrate that the primary crust of Mars is overwhelmingly basaltic in composition [61] (Refer to Figure 4). These expansive tholeiitic basalts lean heavily toward intermediate basaltic andesites or andesites enriched in incompatible and heat-producing elements (e.g., K, Th, and U), crystallizing early in the planet's history during the Noachian epoch [63]. Recent exploration has confirmed the presence of evolved, silica-rich lithologies that break from this basaltic baseline. Notably, dacitic lava flows derived from intensive, localized fractional crystallization have been mapped within the Nili Patera caldera of the Syrtis Major volcanic province [64]. The petrogenetic origin of the primary Martian basaltic crust remains a subject of ongoing debate. Current hypotheses attribute its formation either to the adiabatic decompression and partial melting of ascending mantle plumes or to the large-scale melting of a primitive, fertile mantle driven by internal radiogenic heating [65].

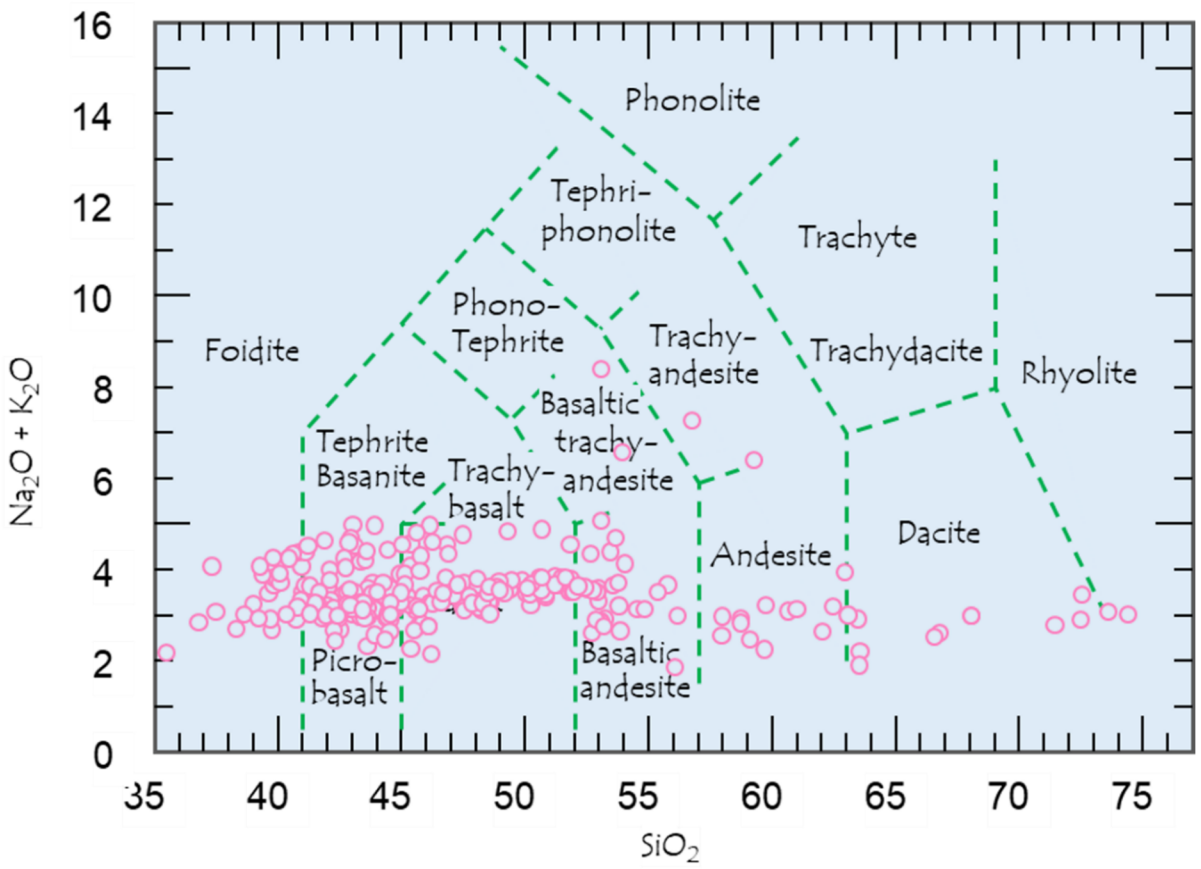

Figure 4. Total Alkali-Silica (TAS) diagram for Martian rocks, showing a predominantly mafic to basaltic composition, with localized ultramafic enrichment (based on 310 sample datasets from sol3905-sol4352 accessed from NASA Planetary Data System—MSL APXS datasets 2025 [66,67]).

Texturally, Martian volcanic units are divided into fine-grained aphanitic flows and porphyritic variants containing distinct phenocryst assemblages [61]. Beyond standard basalts, highly alkaline volcanic suites have been confirmed across several landing sites. In Gale Crater, the Curiosity rover encountered fractional crystallization products including hawaiites and mugearites that exhibit extreme enrichments in iron and total alkalis [68]. Associated sub-volcanic floats include fine-grained monzonitic and coarse-grained dioritic variations, alongside distinct rocks containing prominent alkali feldspars, revealing a complex history of crustal differentiation or localized melting of an alkali-enriched mantle source [69]. Similarly, the Spirit rover identified alkaline volcanic suites within the Columbia Hills of Gusev Crater, recording distinctive plagioclase accumulation over mafic phases [70].

High-resolution orbital data from the Compact Reconnaissance Imaging Spectrometer for Mars (CRISM) has mapped isolated, light-toned bedrock outcrops within Xanthe Terra, crater rims, and deeply eroded exposures across the southern highlands [71]. These units display a diagnostic 1.25–1.3 µm absorption band indicative of minor Fe^{2+} trace substitution within nearly pure plagioclase matrices, confirming the existence of anorthosites and related plutonic granitoid complexes [72,73]. These highly feldspathic, calcium-rich formations (ranging from andesine to anorthite; An_{50} to An_{90}) demonstrate that Mars underwent prolonged, deep magmatic differentiation akin to early lunar or terrestrial crustal flotation mechanisms [73]. This differentiated framework is further validated by the Martian meteorite record, which archives diverse cumulate rocks including orthopyroxenites, clinopyroxenites, and diabases, showcasing a broad spectrum of intrusive and extrusive mafic regimes [60,74,75].

5.2. Mantle Heterogeneities and Metamorphic Paradigms

The petrogenesis of the Martian basaltic crust is intrinsically linked to the long-term thermochemical evolution of a highly heterogeneous mantle [75]. Isotopic decoupling observed across the SNC meteorite suites (specifically U-Pb, Sm-Nd, and Lu-Hf systematics) demonstrates that the Martian mantle separated into distinct, geochemically isolated isotopic reservoirs within the first 50 million years of Solar System history during the crystallization of a primordial global magma ocean [60,76]. Unlike Earth's mantle, which is continuously homogenized via convective mixing driven by active plate subduction, the Martian mantle remained un-mixed [77]. This lack of dynamic recycling

preserved extreme geochemical reservoirs, ranging from a highly depleted, light rare-earth element (LREE) poor shergottite source to an enriched, volatile-bearing nakhlite mantle source province [52,60].

This lack of active plate boundaries fundamentally dictates Mars' metamorphic geology, creating a structural framework that contrasts sharply with Earth's subduction-driven regional metamorphic belts [77]. On Earth, tectonic collisions subject expansive crustal blocks to high-pressure, low-temperature transitions, such as blueschist and eclogite facies transformations [78]. Whereas, on Mars, regional orogenic metamorphism is completely absent. Instead, the Martian metamorphic record is dominated by two localized mechanisms: impact metamorphism and hydrothermal metasomatism [78].

Impact metamorphism occurs during hyper-velocity bolide collisions, exposing the target igneous bedrock to transient shock pressures exceeding 30 to 50 GPa [79,80]. This kinetic energy induces solid-state phase transformations, notably shock-melting calcic plagioclase into isotropic maskelynite glass and forcing the mechanical deformation of pyroxenes features that define the highly shocked shergottite and chassignite matrices [53,54]. Concurrently, localized hydrothermal metamorphism operates around deep impact craters and active volcanic centers [81]. In these zones, circulating, volatile-rich subsurface groundwaters drive autometasomatic alteration, altering primary olivine and pyroxene frameworks into chlorites, serpentines, talc, and epidote matrices [46,81]. This hydrothermal loop provides localized zones of fluid-rock equilibration without needing tectonic burial, creating stable chemical environments in the shallow crust [78].

6. Internal Geophysical Architecture of Mars

To understand the divergent evolutionary paths of Earth and Mars, evaluating their internal differentiation and geophysical stratification is paramount. While early structural models relied heavily on moment of inertia equations derived from orbital tracking, NASA's In-Sight mission, utilizing the Seismic Experiment for Interior Structure (SEIS), provided the first direct seismological mapping of the Martian interior, revealing a structurally distinct crust, an expansive lithospheric mantle, and a uniquely low-density core (Refer to comparative Figure 5).

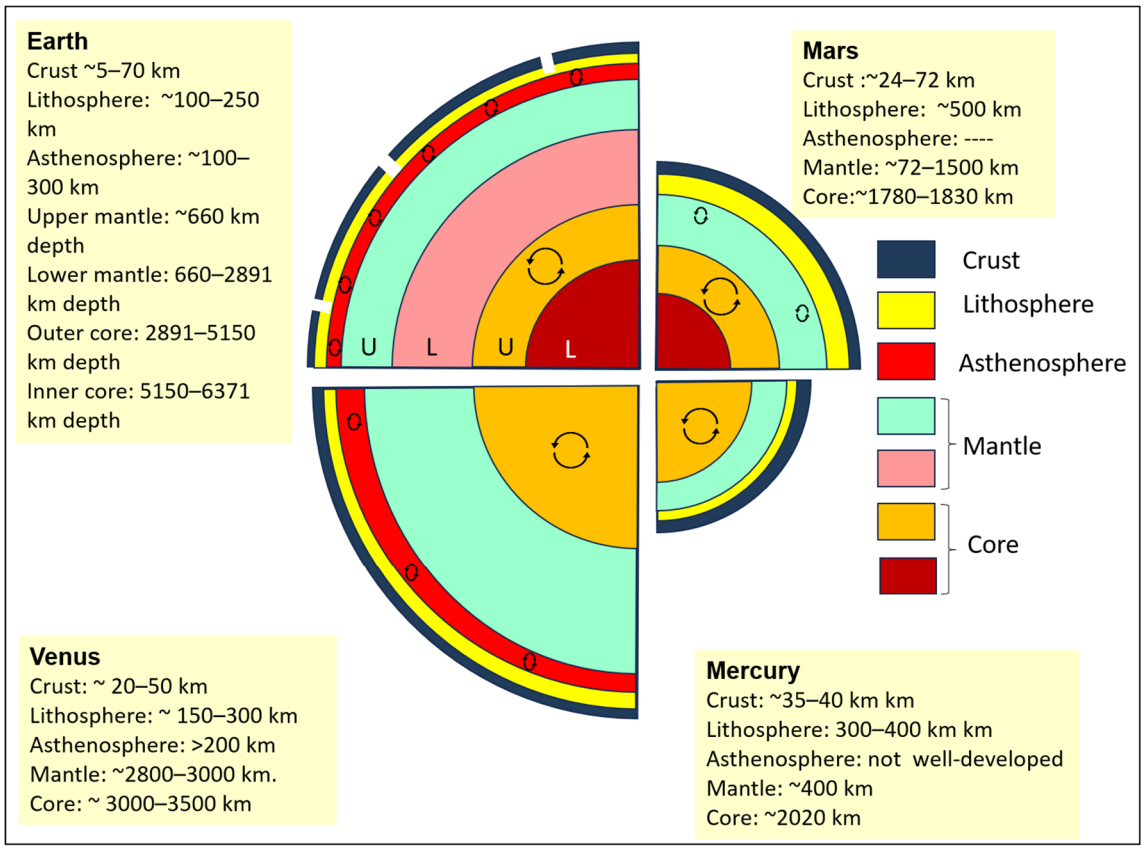

Figure 5. A comparison of the interior of inner planets (modified after [82–88].

6.1. The Martian Crust and Lithospheric Asymmetry

Seismological reflections from low-magnitude marsquakes demonstrate that the Martian crust is significantly thicker and more porous than Earth's ocean-buffered crust. The global average crustal thickness is constrained

between 24 and 72 km, reaching its thinnest baseline (~6 km) beneath the Isidis impact basin and its absolute maximum (~117 km) beneath the southern Tharsis plateau [82]. Recent 3D seismic inversions confirm that the crust is structurally stratified into a high-silica upper layer and a denser, iron-magnesium rich lower layer, bearing indicators of complex ancient rock recycling and massive localized intrusive magmatism [82].

A defining geophysical feature of Mars is its crustal dichotomy the sharp topographic and structural division separating the flat northern lowlands from the heavily cratered, elevated southern highlands [89,90]. Recent dynamic models mapping tidal deformations and k_2 Love number variations have exposed a massive, deep-seated thermal anomaly directly beneath this dichotomy. This structural divide indicates that the southern mantle remains considerably hotter and partially molten compared to the north, suggesting that asymmetric mantle convection or a colossal, ancient hemisphere-scale impact fundamentally locked Mars into a permanent geomorphological imbalance early in its history [39,83,90]

6.2. The Rigid Mantle and Absence of Plate Tectonics

The Martian mantle extends roughly 1560 km beneath the crustal boundary, terminating at the core-mantle interface. Unlike Earth's mantle, which features a prominent asthenosphere driving mobile plate tectonics, the Martian mantle is characterized by an exceptionally deep, rigid lithosphere extending down 400 to 600 km, making it two to three times thicker than Earth's equivalent layers [84]. This immense, cold lithospheric anchor suppresses vigorous mantle overturning, directly explaining why Mars features fixed, long-lived hotspots (allowing volcanoes like Olympus Mons to grow to gargantuan scales over single mantle plumes) rather than lateral plate boundaries. Geochemically, the upper mantle is highly enriched in iron oxide (FeO) with a standard olivine composition averaging Fo_{75}, establishing a denser mantle baseline that dictates the high iron content observed in surface basalts [84].

6.3. The Core: New Insights into Inner Core Crystallization

Foundational analysis of InSight datasets originally modeled the Martian core as a massive, entirely molten metallic sphere spanning roughly half the planet's radius (1830 ± 40 km) [91]. Because this early radius configuration yielded an unexpectedly low bulk density, geophysicists concluded that the core must be heavily enriched in light alloying elements, postulating a mix of 10% to 15% sulfur by weight, alongside trace fractions of oxygen, carbon, and hydrogen [91]. However, recent milestone seismic re-evaluations have completely redefined this paradigm. By analyzing complex seismic wave phase reflections passing directly through the deep planetary center, researchers successfully mapped two core-transiting wave phases (PKKP and PKiKP) that demonstrate Mars possesses a solid, crystalline inner core with a radius of approximately 613 ± 67 km, surrounded by a liquid metallic outer core [92]. This discovery resolves a long-standing mystery regarding planetary cooling: Mars has actively entered its core crystallization epoch. As iron solidifies out of the core fluid, it triggers compositional convection [92]. However, because this crystallization process is insulated by the thick, basal layer of molten silicates at the mantle's floor, the core-mantle heat flux remains too low to restart the global dipolar geodynamo [39]. Consequently, the modern core remains trapped in a state of stagnant convection, preserving an inner solid core but failing to project a global magnetic shield into space [39,92].

7. Sedimentation on Mars

Mars archives an expansive, remarkably preserved stratigraphic record of sedimentary rocks characterized by distinct depositional architectures, varying lithofacies, and complex mineral assemblages [89,93,94]. Due to the absence of persistent plate tectonics and associated crustal recycling, Noachian and Hesperian sedimentary sequences remain pristine preserving surface evolutionary records that predate the oldest surviving sedimentary strata on Earth [95]. Despite this long-term stability, the global rock cycle operates continuously, driving the classic sequence of physical and chemical weathering, erosion, hydrodynamic transport, and diagenetic lithification [95]. This is stratigraphically expressed through complex superpositions where edge-bounded, well-stratified sequences unconformably overlie heavily cratered ancient basement rock [94]. Surface transport is primarily governed by aeolian and paleohydrological regimes, yielding diverse fluvial, lacustrine, and sand-dune deposits across varying spatial scales [93,96–98].

Sedimentary accumulations manifest both as localized depocenters and regional, basin-scale blanket deposits. Localized sedimentation is typified by intra-crater alluvial fans, prograding deltaic wedges, and deep lacustrine beds confined within impact structures and structural grabens, whereas regional mass transport is documented by expansive circum-Chryse outflow channel networks [94] (Refer to Figure 6). Early sediment production was dominated by impact-generated fallback breccias and pyroclastic airfall, which were subsequently reworked by wind and water. These sediments preferentially filled topographic lows, classifying depocenters into underfilled

basins and overfilled craters. Underfilled structures such as Jezero Crater, Holden Crater, and Melas Chasma contain integrated fluvial valley networks terminating in prominent deltas and fine-grained distal lacustrine floor beds [3,6,94]. Furthermore, expansive prograding deltaic wedges distributed along the northern plains boundary suggest the historical presence of a transient, hemisphere-scale Noachian ocean [99]. In Holden Crater, coalescing alluvial fans merge into extensive bajada complexes, recording high-energy, episodic mega-flooding events [3].

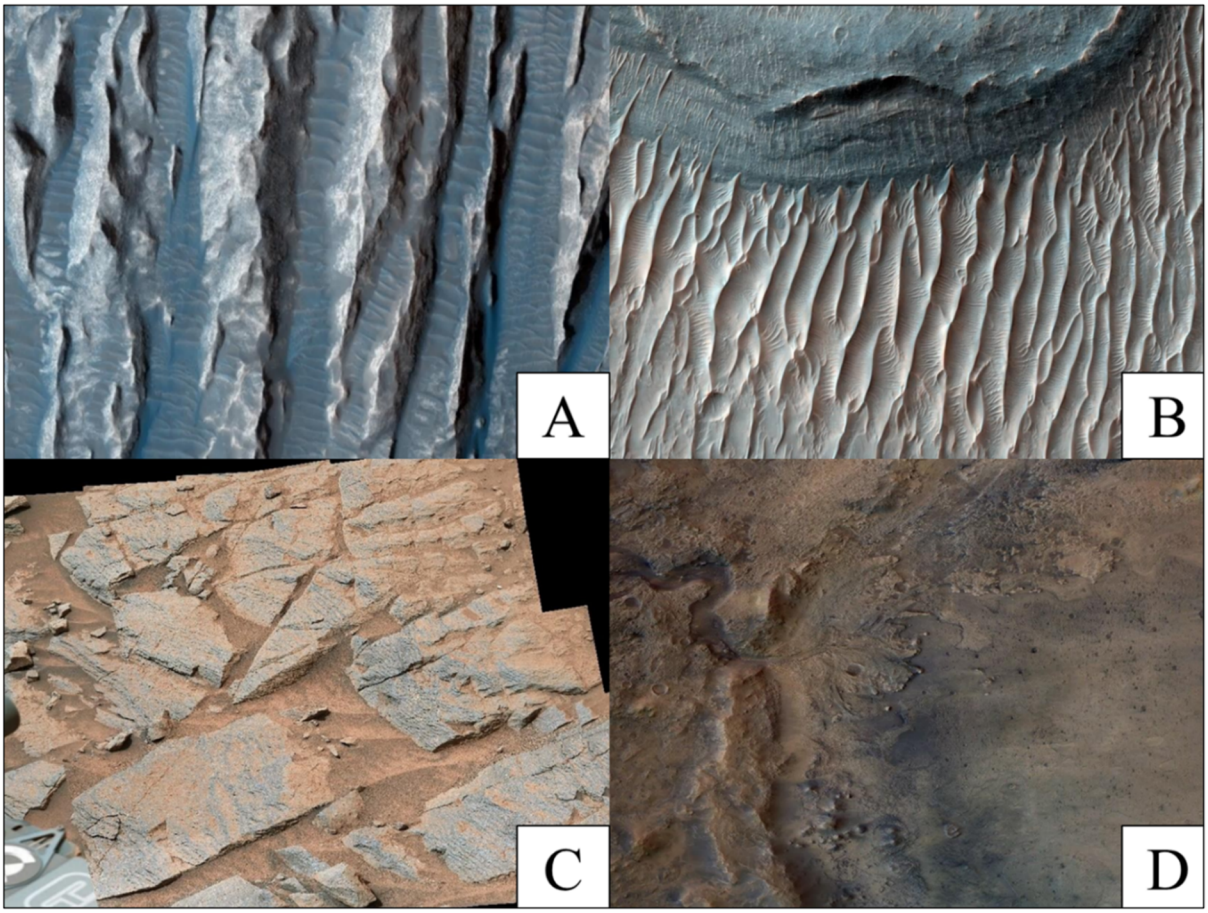

Figure 6. (**A**) Yardang-like features in the Arsinoes Chaos region of Mars, located on the eastern side of the Valles Marineris canyon system, were captured by NASA's Mars Reconnaissance Orbiter using the HiRISE camera on 4 January 2015, at a resolution of 20,000 × 40,000 pixels (Adapted from [100]. Copyright 2015, NASA/JPL-Caltech/Univ. of Arizona), (**B**) Fine stratified layers in the Ius Chasma canyon, also part of Valles Marineris, were imaged by the Mars Reconnaissance Orbiter, revealing sedimentary layers formed by wind and water (Adapted from [101]. Copyright 2008, NASA/JPL-Caltech/Univ. of Arizona), (**C**) Rhythmic bedding structures in Martian sedimentary rocks were photographed by the Curiosity rover using a 2-megapixel camera with a resolution of 1600 × 1200 pixels (Adapted from [102]. Copyright 2023, NASA/JPL-Caltech/MSSS), (**D**) An image of the ancient delta in Mars' Jezero crater was captured by the ESA Mars Express orbiter at a resolution of 10–30 m, highlighting one of the key features of past water activity on the planet (Adapted from [103]. Copyright 2021, ESA/DLR/FU-Berlin).

Conversely, closed-system impact basins like Gale Crater function as internally draining, topographically closed endpoints lacking diagnostic outlet channels. Gale represents an over-accumulated basin sequence, where long-term sedimentary input outpaced localized subsidence [94]. This high-volume influx generated a centralized, 5-km-high sedimentary mound Aeolis Mons preserving rhythmic, climbing cross-stratification that vertically scales near or above the localized regional rim baselines, documenting prolonged, multi-phase aeolian and lacustrine deposition cycles within a closed crater boundary [94]. Regionally, deep troughs like Valles Marineris and Maja Valles bisect the ancient crust, preserving stacked, highly altered geomorphological terraces and modern slope gullies [97,104]. Aeolian transport is equally evident, documented by cross-bedded sandstones, localized interdune fields, and sulfate-rich sand sheets at Meridiani Planum, where fluctuating, highly acidic groundwaters precipitated thick sequences of ferric sulfates [96,105].

Because the primary Martian crust is geochemically basaltic, its subsequent epiclastic derivatives retain a fundamentally mafic mineral signature [61]. Fluid-rock interactions and groundwater-driven diagenesis altered

these source rocks into distinct chemical sediments depending on ambient fluid chemistries. Early, near-neutral pH groundwater networks facilitated the hydrolysis of basaltic glass into widespread phyllosilicates (clays) and localized carbonates; subsequent environmental transitions toward hyper-acidic, sulfur-rich waters precipitated extensive magnesium, calcium, and iron sulfates alongside iron oxides, as mapped by orbital mapping spectrometers like OMEGA and CRISM [106–109].

In-situ examination by the Curiosity rover at Yellowknife Bay within Gale Crater exposed an ancient, long-lived fluvio-lacustrine system composed of fine-grained mudstones and siltstones rich in authigenic saponitic smectite (~20 wt%) derived from sub-aqueous basalt weathering [110]. This paleolake was characterized by neutral pH conditions, low paleosalinity, and distinct, vertically stratified redox pairs, representing a prime habitat capable of sustaining ancient chemolithoautotrophic microbial life [110]. Certain chemical sediments were subsequently reworked by late-stage, localized groundwater surges, inducing the precipitation of secondary crystalline hematite beds under specific fluid-redox stratifications [99,110].

Furthermore, Curiosity detected distinct generations of spherical, millimeter-scale nodules embedded within the mudstone matrices, which represent early diagenetic concretions precipitated from mineral-rich groundwaters flowing through porous sediment pore-spaces. Many of these nodules display hollow cores, indicating either the dissolution of highly soluble early mineral phases or trapped diagnostic gas bubbles. Late-stage diagenetic fluids subsequently generated cross-cutting calcium sulfate fractures that partially intersect and fill these nodules, documenting a complex, multi-phase history of subsurface aqueous flow long after primary lake desiccation [110]. As global volcanic and impact rates waned heading into the Amazonian epoch, surface liquid water vanished, drastically shifting Mars from a hydrodynamically driven sedimentary loop into a hyper-arid, slow physical weathering regime dominated exclusively by modern global aeolian abrasion [61].

8. Surface Mineralogical Mapping of the Martian Surface

Mars owes its diagnostic visible spectrum and high surface albedo to a ubiquitous cover of fine-grained global dust enriched in nanophase ferric oxides, such as amorphous np-Fe_2O_3 (nanophase-Fe_2O_3), hematite, and maghemite [111]. These oxides exert an intense charge-transfer absorption band at ultraviolet-to-visible wavelengths (<0.55 μm) and a characteristic crystal-field absorption feature near 0.86 μm [111]. High-resolution orbital imaging spectroscopy utilizing Visible-Near Infrared (VNIR) and Thermal Infrared (TIR) mapping methods reveals that beneath this dust mantle, the planetary crust is predominantly composed of primary mafic minerals that have undergone variable post-crystallization aqueous alteration [2]. Over the last two decades, a continuous influx of high-resolution data from hyper-spectral orbiters and *in-situ* rover laboratories has profoundly advanced our understanding of these mineral systems [112].

Utilizing orbital hyperspectral mapping spectrometers like OMEGA and CRISM, researchers have cataloged distinct regional mineral belts [71,113]. These global inventories reveal diverse mineral suites, including:

(i) Primary Mafic Frameworks: Coarse-grained olivine, clinopyroxene (augite), orthopyroxene (pigeonite), and calcic plagioclase, marking expansive volcanic flows and impact melt sheets [60,112].
(ii) Phyllosilicates (Clays): Widespread iron-magnesium smectites (nontronite, saponite), aluminum phyllosilicates (kaolinite, halloysite), and deep-seated chlorite and serpentine matrices [81,114].
(iii) Sulfates and Halides: Localized deposits of gypsum, jarosite, kieserite, and polyhydrated sulfates, registering high-solute evaporitic trends [108].
(iv) Carbonates and Zeolites: Isolated occurrences of calcite, magnesite, analcime, and prehnite, recording constrained neutral-to-alkaline aqueous environments [113,114].

This diverse surface mineralogy functions as a high-fidelity record of ancient planetary climates [113]. While the primary mafic phases record vigorous magmatic and impact cycles, the interbedded hydrous silicates, sulfates, and carbonates document extensive, long-term fluid-rock interactions [109,113]. For example, localized serpentine and chlorite assemblages provide direct thermodynamic evidence of past subsurface hydrothermal networks [81]. Furthermore, evaporitic sulfate and chloride basins carry critical astrobiological significance. These structures act as prime targets for biosignature preservation, as salt matrices efficiently shield delicate macromolecular organic chains and microbial remains from destructive ambient cosmic radiation [115]. Concurrently, terrestrial analogs demonstrate that specialized halophilic microorganisms can survive under extreme desiccation and freezing cycles within fluid inclusions in these exact salt structures, establishing them as key astrobiological focus zones [116]. Because Mars preserves these Noachian and Hesperian terrains without the destructive erasing forces of plate tectonics or persistent biogenic overprinting, its mineral record provides an unparalleled window into the prebiotic chemical environments that preceded the origin of life on early Earth [114,117].

Unambiguous geomorphological and spectral data show that the distribution of these hydrous minerals varies drastically across planetary timelines [109]. The vast majority of Martian Fe/Mg-smectites are strictly restricted to ancient Noachian basements (~3.7 Ga), recording low water-to-rock ratio (W/R) interactions with deep, insulated hydrothermal aquifers rather than open-system atmospheric precipitation or sub-aerial weathering [109,113]. Conversely, surface water activity peaked transiently during the late Noachian to early Hesperian transition, driven by episodic, impact-induced or volcanically forced ice-melting events that cut widespread valley networks and deposited regional sulfate sheets under increasingly arid and acidic atmospheric conditions [108,118]. Today, next-generation surface payloads like the SHERLOC (Scanning Habitable Environments with Raman and Luminescence for Organics and Chemicals) instrument aboard the *Perseverance* rover are operating at sub-millimeter scales, isolating trace organic carbon rings directly tucked within these crystalline mineral boundaries [119]. Ultimately, these multi-scale datasets strongly converge on an evolutionary model where Mars' long-term, sustained habitable environments were primarily subsurface, chemically closed, and hydrothermally driven offering stable, long-lasting thermodynamic niches shielded from the increasingly lethal, hyper-arid surface radiation regimes of the maturing planet [109].

9. Geomorphological Features

Mars displays a diverse array of macro-scale geomorphological features driven by stark regional variations across its northern and southern hemispheres, dividing the planet into distinct highlands, lowlands, and complex volcano-tectonic provinces [120]. The northern hemisphere is dominated by the vast, low-albedo plains of Vastitas Borealis, which contain several deep impact structures including Lyot and Korolev craters. These impact basins provide critical windows into the shallow sub-surface stratigraphy, with Jezero Crater serving as a prime example; its well-preserved lacustrine floor and clay-bearing deltaic packages provided the first unambiguous evidence of long-term fluvio-lacustrine activity [94,120].

In contrast, the southern hemisphere features a rugged, crater-thickened, and topographically elevated crust [120]. This hemisphere hosts the massive Valles Marineris canyon system the largest extensional graben network in the Solar System and the sprawling Tharsis bulge, which supports gargantuan shield volcanoes such as Olympus Mons [104,121]. Expansive valley networks, including Ma'adim Vallis, Mawrth Vallis, and Valles Alpes, trace long-term fluid transit pathways across these highlands [118,122]. Structural deformation is extensively recorded by networks of fossae, which are elongated, narrow graben depressions radiating outward from the Tharsis volcanic center [123]. Additional volcanic features include Syrtis Major, a broad Hesperian-aged volcanic plain composed of low-viscosity basaltic flows [64]. The southern crustal template is bounded by Hellas Planitia and Argyre Planitia, two colossal impact basins that host thick sequences of flat-lying sedimentary and volatile-rich floor deposits [120].

9.1. Martian Valleys

While contemporary Mars behaves as a hyper-arid, frozen desert, its ancient highland crust preserves a starkly different paleoclimate baseline characterized by active surface fluid dynamics. Morphological remnants of paleolakes, dendritic channels, highly modified crater rims, and prograding delta fans record an active hydrologic cycle extending from the late Noachian to the early Hesperian epoch, approximately 3.7 to 4.0 Ga [118,124]. Widespread valley networks display interconnected, branching tributaries originating near prominent drainage divides [118]. Early planetary models attributed these high-order branching systems exclusively to groundwater sapping mechanisms [125]. However, cross-cutting profiles reveal that many southern highland valley systems are structurally less mature and exhibit lower drainage densities compared to mature terrestrial networks [122]. This indicates that surface runoff driven by precipitation did not persist long enough to fully grade the cratered landscapes [124].

To resolve these formation mechanisms, researchers have mapped these global networks, evaluating competing hypotheses of pluvial surface runoff, groundwater sapping, and subglacial melting [122]. A major paradigm shift introduced by [6] demonstrated that many branching systems match the morphology of subglacial channels in the Canadian Arctic Archipelago, proving that subglacial meltwater drainage beneath extensive ice sheets rather than open-system rainfall incised these highland networks under a cold, icy early climate

Chronologically, global synthesis models demonstrate that peak valley network incision abruptly ceased near the Noachian-Hesperian boundary, transitioning from fluvial downcutting (~0.25 meters per million years) to hyper-arid background erosion regimes. The structural framework of these valleys is further complicated by volcano-tectonic overprinting [121]. Extensional Grand Canyon systems like Valles Marineris opened primarily via extensional tectonic rifting driven by lithospheric stress from the loading of the Tharsis bulge [121], or

collapsed via mantle plume loading [104]. Both models agree that initial structural fracturing was subsequently amplified by intense mass wasting, fluvial erosion, and aeolian deposition [104,121].

The stratigraphically youngest indicators of transient fluid activity manifest as pristine slope gullies, which form highly incised alcove-channel-apron networks cut directly into steep intra-crater walls. These features point to transient liquid water flows or dense carbon dioxide frost flows occurring within the last few million years [126,127]. This implies that active deep aquifers remain trapped beneath a thick, global planetary cryosphere that effectively seals the deep-seated groundwater table from the hyper-vacuum conditions of the modern Martian surface [127].

9.2. Impact Cratering

Impact craters represent fundamental, multi-scale geomorphological structures formed via the hyper-velocity kinetic excavation of planetary surfaces by meteoritic, asteroidal, or cometary debris. While thick planetary atmospheres can filter or fragment small incoming bolides, Mars' hyper-attenuated modern atmosphere permits an extensive flux of small-scale impactors to reach its surface [128]. These craters serve as invaluable tools for comparative planetology, providing critical constraints on surface absolute ages, historical volatile distributions, and long-term degradation rates [120]. To date, more than 42,000 impact structures with diameters exceeding 5 km have been officially cataloged across Mars, with sub-kilometer features numbering in the millions. Preeminent examples include the massive multi-ring impact basins of Hellas, Argyre, Isidis, and Utopia, alongside heavily modified complex structures such as Huygens, Schiaparelli, Greeley, and Cassini [120].

Due to its low global erosion rates, Mars is a premier laboratory for crater statistical analysis (crater counting methods), as it uniquely preserves surface units spanning the Noachian, Hesperian, and Amazonian epochs [120]. This crater distribution clearly exposes the planet's fundamental crustal dichotomy. The topographically depressed northern lowlands display a significantly lower crater density compared to the heavily fractured southern highlands, recording a much younger geological retention age. This asymmetry is attributed either to ancient, overlapping mega-impacts [129] or to a singular, hemisphere-scale Noachian impact event [90]. The bulk of the Martian megaregolith was produced during this early phase of intense bombardment, culminating in the Late Heavy Bombardment (LHB) approximately 3.8 billion years ago. Since the cessation of the LHB, the core morphological features of mid-to-high latitude craters have remained stable due to an overall drop in global surface degradation [120].

Topographic soundings from the Mars Orbiter Laser Altimeter (MOLA) and subsurface radar profiles from the Mars Advanced Radar for Subsurface and Ionospheric Sounding (MARSIS) have mapped thousands of "quasi-circular depressions" (QCDs) [89]. These represent an ancient population of deeply buried impact craters completely hidden beneath the volcanic flows and sedimentary blankets of the northern plains.

Furthermore, crater modification patterns vary systematically with latitude. In mid-latitude zones, complex craters exhibit widespread "terrain softening" (a specialized creep-induced degradation process where steep topography undergoes viscous relaxation within an ice-rich megaregolith, yielding characteristically rounded rims and lobate debris aprons along crater floors [130]). Extending this model to the polar regions, numerical finite element models published by Pathare et al. (2005) demonstrate that craters within the polar layered deposits are modified almost exclusively by the long-term viscous creep relaxation of dusty water ice, meaning that crater depth-to-diameter ratios function as an indirect thermometer for past planetary ice sheet dynamics rather than simple sub-aerial erosion [79,131].

Beyond functioning as simple age markers, impact events play a dynamic role in altering localized geology. High-velocity collisions release immense shock waves and seismic energy, driving localized structural deformation and triggering fluidization patterns within volatile-bearing target materials. The fresh complex craters of Mars are uniquely characterized by layered, lobate, or "rampart" ejecta blankets that terminate in distinct distal ridges. These structures form when the high-velocity impact melt interacts with subsurface groundwater or cryospheric ice lenses, converting the ejected debris curtain into a hyper-concentrated mudflow that sweeps radially outward [80,132,133]. The structural preservation of these distinct ejecta blankets and associated central floor pits provides global proof that Mars maintains a volatile-rich, highly icy shallow crust [120].

10. Chronological Studies of the Martian Subsurface

Establishing an absolute planetary chronology for Mars relies heavily on crater size-frequency distribution (CSFD) modeling, a remote-sensing geomorphological method subject to significant uncertainties regarding impactor flux calibrations and localized surface overprinting. To calibrate this cratering timeline precisely, deriving direct radiometric crystallization ages from *in-situ* or returned Martian rock samples remains paramount [134,135]. Based

on global CSFD statistical mapping, Martian geological and stratigraphic history is systematically partitioned into three master chronographic epochs: the Noachian, Hesperian, and Amazonian [76].

(a) The Noachian Epoch (Pre-3.7 Ga): Spans roughly 40% of the preserved surface, encompassing the initial solidification of the primary basaltic crust [136]. This early window was characterized by extreme impact flux rates culminating in the Late Heavy Bombardment (LHB) which induced widespread crustal fracturing, high-energy impact excavation, and rapid crater degradation driven by a transiently thicker atmosphere [120].
(b) The Hesperian Epoch (3.7 to 3.0 Ga): Covers approximately 34% of the planetary surface area. This transitional period records a sharp drop in impact cratering rates but features a dramatic surge in global effusive plains volcanism and catastrophic outflow channel flooding events [137].
(c) The Amazonian Epoch (3.0 Ga to Present): Accounts for the remaining 26% of the surface template [137]. Impact craters formed during this modern era exhibit minimal post-depositional degradation, reflecting an exceptionally calm geomorphic regime [5]. Global erosion rates during the Hesperian-Amazonian hyper-arid baseline dropped to a nominal 0.1 to 10 nanometers per year [138].

Within the rugged, ancient southern hemisphere, the Early Noachian is recorded by thick, high-relief massifs framing the rims of the colossal Hellas, Argyre, and Isidis impact basins [132,139–141]. Early Noachian depositional blocks present heavily degraded geomorphologies composed of complex breccia matrices, early volcano-sedimentary layers, and fluvial valleys incised during brief windows of precipitation and high-velocity runoff. These basement rocks were subsequently blanketed by widespread Late Noachian to Early Hesperian intercrater plains deposits. Long-term erosion degraded these early units into scattered knobby terrains, while distinct contractional wrinkle ridges and horizontal structural benches ring the margins of the northern lowlands and the Hellas basin geomorphological indicators interpreted by some planetary models as ancient paleo-shorelines [63,142].

Conversely, Noachian-aged exposures are heavily buried and significantly less abundant across the northern lowlands. The oldest accessible material in the north dates to the Late Noachian or Early Hesperian transition, manifesting as isolated, high-standing knobby outcrops along the junctions of Elysium, Amazonis, and Arcadia Planitiae, alongside a massive, highly altered structural mesa within Acidalia Planitia [143,144]. Hesperian plains deposits display gentle, uniform slope profiles.

Geomorphologically, these terrains present isolated knobby fields indicative of widespread subsurface disruption and cryovolcanic mass wasting. These irregular arrays are structurally juxtaposed against vast, un-cratered smooth regions planated by episodic, high-energy outflow channel discharges, low-viscosity sheet volcanism, and seasonal periglacial cryoturbation [135,144]. Finally, the modern Amazonian record marks the final transition into a hyper-arid world. Rather than ocean sediments, Amazonian units are dominated by localized volcanic flows, widespread gravity-driven debris aprons, and global polar-to-mid-latitude cryospheric dust-ice mantles shaped by modern wind patterns [145].

11. In Search of Life on Mars

Ancient Martian terrains dating from the Pre-Noachian to Noachian epochs preserve extensive evidence of stable surface paleohydrology and localized marine-like environments [94,143]. These systems serve as direct geomorphological and geochemical analogues to the sub-aqueous volcanic and hydrothermal fields that supported early microbial life on Earth [146]. Within these frameworks, ancient hydrothermal centers played a critical role in enhancing astrobiological preservation potential [147]. Rapid mineral precipitation and silica cementation within these settings effectively entombed delicate cellular architecture before environmental degradation took effect [146,147]. Consequently, comparative planetology supports targeted exploration matrices prioritizing localized sedimentary successions within ancient hydrothermal vents specifically horizons rich in opaline silica and high-surface-area phyllosilicates intimately associated with localized volcanism [147].

Because the contemporary surface is bombarded by lethal ionizing radiation and cosmic rays, prospective traces of Martian life are heavily shielded, favoring deep subsurface sanctuaries, sub-surface rock shelters, or localized mineral matrices rich in crystalline iron oxides (such as hematite) [148]. Laboratory simulations demonstrate that terrestrial endoliths including highly resilient bacteria, cyanobacteria, and lichens can survive simulated Mars-like environmental stresses when physically shielded by a few millimeters of rocky regolith [148]. Under active metabolic regimes, localized mineral suites composed of secondary carbonates and iron-calcium sulfates can precipitate via microbial respiration mechanisms [149,150].

For example, specialized anaerobic sulfate-reducing bacteria and iron-reducing chemolithotrophs exploit metabolic redox couples to actively dissolve and re-precipitate secondary iron oxide and carbonate matrices [150]. This processing triggers intense, diagnostic stable isotope fractionation patterns specifically generating wide, non-equilibrium stable sulfur isotope ($\delta^{34}S$) variations that differ fundamentally from baseline abiotic values [150].

This biological activity generates dense networks of Extracellular Polymeric Substances (EPS) that accelerate parent rock leaching, leaving behind specialized indicators that can persist long after biological death, making high-density hematite formations primary targets for *in-situ* biosignature tracking [151].

11.1. Morphological Pareidolia and Optical Resolution Constraints

Astrobiological investigations track a broad spectrum of potential life detection matrices, broadly categorized into morphological, organic macromolecular, and elemental/isotopic biosignatures [147]. Morphological signatures are defined by physical cellular structures, structured filamentous geometries, or macro-scale mineral textures explicitly generated by biological ordering [152]. However, morphology is widely considered the most ambiguous and least secure line of evidence in life-detection paradigms [153].

Within Gale Crater, speculative claims have emerged analyzing ground images captured by the Curiosity rover's Mars Hand Lens Imager (MAHLI). These interpretations argue for the presence of microstructures mimicking terrestrial green algae (*Nostoc* or *Oedogonium* templates) containing specialized reproductive structures like oogonia. However, an evaluation of the physical optics and instrument payload mechanics demonstrates that these biogenic claims are physically impossible. The MAHLI camera system is engineered to deliver a maximum spatial resolution of approximately 20 μm per pixel at its closest working distance (~2.1 cm from the target lens to the bedrock surface). Within digital imaging and planetary petrology, securely identifying a complex, diagnostic biological feature requires a minimum spatial grid of 5 × 5 pixels to reliably isolate structural features from the surrounding matrix, establishing a firm identification threshold at features larger than 100 μm. Because diagnostic terrestrial algal structures like oogonia typically measure under 70 μm in length, they fall entirely beneath the physical resolution limits of the instrument. At these micro-scales, a feature spanning only 2 to 3 pixels cannot manifest resolvable biological features. Consequently, the apparent "cells" and "filaments" highlighted in highly publicized alternative claims represent classic inorganic pseudofossils [153]. These features are fully explained by standard, non-biological sedimentary and igneous processes, including fluid-driven grain sorting, micro-fracturing along basaltic crystal joints, and localized hydrothermal mineral leaching [153].

11.2. Organic and Isotopic Signatures

In contrast to simple shapes, organic biosignatures offer highly secure indicators of past life due to the distinct chemical architectures of molecules shaped by biological synthesis [154]. These include preserved lipid hydrocarbon frameworks, amino acid enantiomeric distributions, and structural isomeric preferences that reflect strict biological selectivity [154]. Determining biological origin relies heavily on tracking molecular structural patterns, such as a strong diagnostic preference for left- or right-handed configurations (enantiomeric excess) or repeating, orderly carbon-chain subunits [154]. Long-term preservation of these labile organic compounds requires rapid burial within low-permeability, fine-grained sediments to shield them from deep solar ultraviolet exposure and heavy oxidizing chemicals [155].

High-priority astrobiological targets include amorphous carbonaceous matter and fossilized EPS matrices, which exhibit superior structural preservation in ancient rocks compared to fragile cellular walls [147]. However, on the modern Martian surface, highly oxidizing compounds (such as perchlorates and hydrogen peroxide radicals) actively destroy surface organic compounds, a challenge that applies equally to biogenic, abiotic, prebiotic, and cosmic meteoritic carbon inputs [147]. This preservation dynamic was vividly illuminated when NASA's Perseverance *r*over discovered the 'Cheyava Falls' bedrock outcrop within the ancient Neretva Vallis river channel of Jezero Crater. Measuring roughly 1 m by 0.6 m, this iron- and sulfate-rich sedimentary rock preserves a highly complex potential biosignature assembly. High-resolution mapping by the SHERLOC and PIXL instruments revealed cross-cutting white calcium sulfate veins sandwiching distinct bands of reddish iron oxides. Crucially, these red bands are heavily interspersed with millimeter-scale, irregular white 'leopard spots' rimmed by dark, ring-like halos.

Elemental maps confirm that these halos are enriched in both iron and phosphorus, surrounding internal matrices loaded with organic carbon rings. On Earth, this exact chemical and spatial arrangement is a classic indicator of microbial reduction loops, where organic matter acts as a biological battery, driving localized redox reactions that convert insoluble Fe^{3+} into soluble Fe^{2+} and leaving behind diagnostic depleted halos. However, because highly energetic, multi-phase hydrothermal fluid flows can abiotically mimic these iron-phosphate reduction rings via complex non-biological mineral leaching, the biogenicity of Cheyava Falls remains highly ambiguous. It stands as a prime example of a 'dubiofossil' that requires direct sample return to Earth to verify via transmission electron microscopy and isotopic nanobeam mass spectrometry.

This preservation contrast is further illustrated by the Martian meteorite record. The famous Noachian orthopyroxenite ALH 84001 preserves complex polycyclic aromatic hydrocarbons (PAHs) intensely concentrated around its internal carbonate globules [156]. Because these PAHs are concentrated deep within the specimen's interior and lack modern terrestrial Carbon-14 signatures, they are confirmed as ancient and pre-terrestrial in origin [156]. Furthermore, these carbonate globules contain highly pure, elongated, and structurally flawless nanometer-scale magnetite (Fe_3O_4) crystals [157]. While initially classified as biogenic "magnetofossils" akin to terrestrial magnetotactic bacterial chains, extensive laboratory simulations have demonstrated that these exact truncated hexa-octahedral magnetite shapes can be produced abiotically via the thermal decomposition of iron-bearing carbonates during impact-induced shock heating [157,158].

This preservation contrast is further illustrated by the Martian meteorite record. The famous Noachian orthopyroxenite ALH 84001 preserves complex polycyclic aromatic hydrocarbons (PAHs) intensely concentrated around its internal carbonate globules [156]. Because these PAHs are concentrated deep within the specimen's interior and lack modern terrestrial Carbon-14 signatures, they are confirmed as ancient and pre-terrestrial in origin [156]. Furthermore, these carbonate globules contain highly pure, elongated, and structurally flawless nanometer-scale magnetite (Fe_3O_4) crystals [157]. While initially classified as biogenic "magnetofossils" akin to terrestrial magnetotactic bacterial chains, extensive laboratory simulations have demonstrated that these exact truncated hexa-octahedral magnetite shapes can be produced abiotically via the thermal decomposition of iron-bearing carbonates during impact-induced shock heating [157,158].

Similarly, the Tissint Martian meteorite preserves a diverse suite of C_3 to C_7 branched carboxylic acids, aldehydes, and organomagnesium compounds concentrated inside shock-melt veins and olivine macrocrystals [159]. High-resolution mass spectrometry (FTICR-MS) and NMR spectroscopy confirm that this molecular diversity represents endogenous Martian carbon, yet its structure points to an entirely abiotic origin [159]. These complex molecules were synthesized via deep-seated electrochemical carbon dioxide reduction, localized serpentinization, and high-temperature fluid-mineral interactions within the Martian crust, demonstrating a rich co-evolution of mineral and organic chemistry without biological intervention [159].

11.3. Elemental and Biominerals Interactions

Elemental abundances, micro-scale chemical distributions, and redox-sensitive element variations form a third pillar in life-detection missions [160,161]. Biological activity alters its immediate chemical matrix by triggering the precipitation of specific mineral phases (biominerals), selectively concentrating trace nutrients, and inducing severe stable isotope fractionation patterns [150,155]. Under Earth-like conditions, active microbial metabolisms generate distinctive minerals like high-magnesium calcite, dolomite, and iron sulfides, while shifting stable sulfur and carbon isotope ratios away from baseline abiotic values [150]. Laboratory simulations mimicking Martian chemical baselines show that cyanobacteria (such as *Lyngbya*) and specialized bacteria (such as *Proteus mirabilis*) can actively force the precipitation of rare phosphate minerals like hazenite and struvite under tight geochemical constraints [162].

Furthermore, experimental simulations mapping the interaction of early biomolecules (such as lecithin) with Martian regolith simulants show that organic decomposition directly controls the resulting structure of secondary carbonates [149]. While tracking large variations in stable sulfur isotopes (such as $\delta^{34}S$ shifts) provides a powerful indicator for biological sulfur cycling, the persistent risk of false positives remains severe [150,153]. In energy-rich, geodynamically active Martian sub-surfaces, self-organizing chemical reactions driven by intense thermal and volcanic gradients can easily generate complex organo-mineral interfaces and isotopic fractionations that perfectly copy biological signatures [153]. Consequently, isolating true biosignatures requires an exhaustive, multi-layered baseline mapping of all possible abiotic pathways before declaring a biogenic origin for any Martian sample [153].

The loss of surface water does not mean Mars is completely dead [163]. While the frozen surface is lethal, the deep underground ice and water layers offer conditions very similar to extreme environments on Earth [163,164]. For example, microbes discovered deep inside rocks in Antarctica's Dry Valleys or kilometers beneath Arctic permafrost survive without sun or air. Instead, they stay shielded from the surface and get their energy entirely from simple chemical reactions with rocks and gases [164]. On Mars, deep-seated regional aquifers, kept liquid by localized radiogenic decay and insulating cryospheric seals, mimic these terrestrial deep biospheres [127,163]. In these zones, anaerobic, chemolithoautotrophic microorganisms resembling terrestrial methanogenic archaea or iron-reducing bacteria could theoretically persist indefinitely [164]. These organisms would utilize volatile hydrogen and carbon dioxide generated via crustal serpentinization to run biological systems completely independent of solar insolation or surface environmental degradation [127,164].

12. Paleoenvironmental Reconstructions

Geomorphological, geochemical, and stratigraphic datasets strongly indicate that early Mars maintained localized, long-term habitable environments within its shallow crust and surface boundary layer [94]. Evaluating the habitability profile of the early Martian system involves reconstructing its integrated planetary volatile inventories, historical atmospheric densities, and active paleohydrological networks [135]. Based on multi-mission datasets spanning Mariner 9*,* the Viking orbiters, and Mars Global Surveyor early comparative planetologists resurrected 17th to 19th century ground-based telescopic hypotheses by identifying massive geomorphological scars left by ancient lacustrine, fluvial, and potentially marine systems [125,165].

Ground-level operations have confirmed these macro-scale orbital models. Ground investigations by the *Curiosity* rover within Gale Crater provided definitive, *in-situ* geochemical evidence of historical habitability pathways, exposing complex networks of gravelly river beds, delta front plumes, and perennially stratified freshwater lacustrine mudstone successions that filled the crater basin for millions of years [110,166]. Global evidence for these sustained paleohydrological systems includes deeply incised outflow channel valleys, dendritic river networks, thick phyllosilicate horizons, and extensive deltaic sequences across various terrains [94,122].

Beyond liquid water systems, extensive cryospheric and glacial features have been mapped across mid-to-high latitudes [24]. The stratified, light-toned sulfate mounds within Juventae Chasma record complex paleoclimatic adjustments, where high-obliquity cycles facilitated the co-deposition of volcanic sulfate aerosols alongside thick glacial ice layers [167]. Similarly, subsurface radar sounding measurements mapping the radar dielectric properties of the sprawling Medusae Fossae Formation and polar layered deposits reveal massive, localized accumulations of dust-shrouded glacial ice and relict permafrost structures [168]. Transient water activity persists into the modern hyper-arid era, expressed as localized slope gullies cut into modern crater walls, indicating brief melting events beneath the sealing boundary layer of the global cryosphere [127]. Expansive lacustrine deposits within isolated structural sinks including the Ladon Basin, Ladon Valles, Holden Crater, and Eberswalde Crater further confirm that ancient Mars supported long-lived sub-aqueous sedimentation traps [169,170].

Quantifying this paleoclimate progression reveals a distinct, stepwise environmental collapse across major geological epochs [94]. During the Noachian epoch, intense impact rates and widespread outgassing sustained an open-system weathering baseline, prompting the formation of iron-magnesium smectites and localized carbonates under neutral-to-alkaline pH levels [109,171]. As planetary geodynamic activity declined heading into the Hesperian epoch, the atmosphere thinned and water chemistry underwent global acidification; high-solute groundwaters dominated by dissolved sulfur species precipitated global sulfate and halide sheets, marking a dry-to-wet transitional climate cycle [105,108]. By the Amazonian epoch, stable, open-system surface liquid water vanished, leaving the planet dominated by hyper-slow, dry sub-aerial weathering [172].

This long-term cooling baseline was interrupted by intense, short-term climatic spikes driven by orbital mechanics. Due to strong gravitational perturbations from Jupiter and the lack of a stabilizing large moon, Mars' obliquity fluctuated chaotically between 0° and nearly 60° (and theoretically up to 80°) over million-year timescales [25]. During intense high-obliquity shifts, the polar caps tilted directly toward the Sun, initiating rapid sublimation that significantly increased global atmospheric pressure, temperature, and relative humidity [17,25]. These orbital spikes triggered widespread melting of glaciers and shallow permafrost, unleashing catastrophic megafloods that temporarily filled massive paleolakes, inland seas, and localized northern ocean basins bounded by distinct, global paleo-shorelines [143,165]. Geodetic mapping demonstrates that these smooth lowland margins remained topographically stable against the rugged southern highlands over extended intervals [165]. As the planet's axial tilt returned to low-obliquity baselines, surface waters rapidly receded, evaporated, and refroze into the subsurface, capturing distinct prograding sedimentary sequences that document a repeating cycle of transient habitability under extreme planetary constraints [172,173].

13. Subsurface Geology and Hydrogeology

Quantifying the modern volatile budget of Mars suggests that while its hyper-arid surface is barren, its subsurface reservoir retains massive volumes of volatile storage. Global remote sensing models estimate that the cryosphere and deep aquifers preserve over 21 million cubic kilometers of water ice, a volume mathematically sufficient to wrap the entire planetary geoid in a global ocean approximately 35 m deep [174]. The structural properties of this deep hydrosphere are directly recorded by Martian achondrite meteorites, which preserve micro-scale geochemical signatures of primary differentiation, ancient subsurface hydrothermal fluid-rock loops, and low-temperature hydration alterations [175,176].

Transient surface fluid expressions such as mid-latitude slope gullies indicate that liquid water or dense volatile slumps occurred within the last few million years, driven by groundwater seepage and localized sapping

along structural headwalls [126,127]. Although ambient temperatures and extreme low pressures preclude long-term surface water stability today, extensive sub-cryospheric groundwater systems remain highly plausible [127]. During warm, high-obliquity paleoclimate windows, atmospheric precipitation and glacial meltwater systematically percolated into the highly fractured megaregolith, charging deep regional aquifers [143]. As the planet cooled and its atmosphere thinned, a global, kilometric-scale cryosphere developed from the top down, effectively sealing and trapping these pressurized aquifers beneath an impermeable permafrost blanket [127].

The structural collapse of this hydrological network was accelerated by long-term atmospheric stripping [177]. Following the early demise of the global dipolar geodynamo, unshielded solar wind interaction drove the photolysis of water molecules in the upper atmosphere, causing rapid hydrogen escape into interstellar space [43]. Crucially, an enormous fraction of Mars' missing water inventory did not escape into space, but was permanently trapped within the crust through massive metamorphic hydration reactions and crustal serpentinization [178]. Because Martian mantle melts are uniquely enriched in iron oxide, Martian lavas contain roughly 25% more FeO than terrestrial basalts [61]. Geochemical modeling demonstrates that this iron-rich crust acts as a highly efficient mineral sponge; chemical weathering and alteration reactions structurally bound massive quantities of water directly into secondary hydroxylated minerals (such as serpentines and chlorites), locking away an ancient water volume equivalent to a global layer hundreds of meters deep [178].

Modern planetary exploration has transitioned into the subsurface using orbital and surface radar sounding profiles [168,179]. The Mars 2020 Perseverance rover pioneered the use of ground-penetrating radar (GPR) on the surface, using the Radar Imager for Mars' Subsurface Experiment (RIMFAX) to map the continuous structural stratigraphy down to depths of 15 m [180]. RIMFAX data revealed heavily dipping basaltic rock layers, uniform sub-surface volcanic cross-bedding, and buried lacustrine strata, providing the first direct ground-truth validation of complex intra-crater sedimentation architectures [180]. These surface soundings complement wider robotic configurations, including the WISDOM high-frequency radar on ESA's ExoMars rover, and the Subsurface Penetrating Radar (SPR) aboard China's Zhurong rover, which collectively map the spatial continuity of shallow permafrost sheets and buried volcanic flows [181]. Modern global tracking estimates that these residual ice reserves represent 5% to 30% of Earth's modern ocean volume, securely tucked away inside the polar layered deposits and deep crustal traps [174,179].

The Martian subsurface has long been considered the most consistently habitable region on the planet, making it a promising site to search for evidence of past or present life [163]. Characterizing the habitability profile of this deep biosphere provides a fundamental benchmark for evaluating rocky exoplanets across the galaxy [163]. If deep drilling arrays eventually isolate deep Martian aquifers that possess the energetic chemical ingredients for life yet remain entirely devoid of biology, it would expose an exceptional evolutionary threshold, prompting researchers to isolate the missing chemical triggers required to spark genesis in rocky interiors [182]. Ultimately, the long-term habitability curve of Mars has been irrevocably dictated by the early loss of its protective magnetic and atmospheric envelopes, proving that atmospheric stability is the primary variable regulating surface fluid lifespans and shielding prospective surface biotas from terminal extinction [163].

14. Remote Sensing for Martian Polar Regions

Deep space tracking datasets spanning Mars Global Surveyor (1999–2006), Mars Express (2003 to present), Mars Odyssey (2001 to present), Mars Reconnaissance Orbiter (2006 to present), the Phoenix Lander (2008), and the Mangalyaan Mars Orbiter Mission (2013) have collectively transformed our understanding of the Martian polar regions [183,184]. Cyclical variations in polar ice and dust fluxes are spectrally inferred from characteristic visible-to-infrared wavelengths, registering long-term changes in solar insolation regimes and volatile availability [185]. Dust-rich layers are generated during intense periods of low ice accumulation or widespread seasonal sublimation, forming high-density lag deposits that manifest as distinct stratigraphic unconformities [186]. Consequently, the internal stratigraphy of the polar caps serves as a high-fidelity geomorphological archive documenting past climate conditions, driven by large, chaotic fluctuations in Mars' orbital elements [187,188].

The Polar Layered Deposits (PLDs) display intricate fine-scale stratification, mapped via high-resolution visible and infrared cross-sectional imaging across open troughs and steep scarps, as well as orbital radar sounding [186]. Despite exhibiting smooth macro-scale topographies, the PLD margins are bounded by steep, vertical scarps up to one kilometer high, presenting localized slope angles ranging from 10° to 90° [186]. A suite of orbiter-based low-frequency radars including MARSIS on Mars Express, SHARAD on MRO, and MOSIR aboard Tianwen-1 profile the deep interior of these sheets, calculating cryospheric water-ice volume budgets and looking for structural geological boundaries [179]. A major point of ongoing scientific debate centers on the potential detection of subglacial liquid water beneath the South Polar Layered Deposits (SPLDs). While early MARSIS radar soundings

identified highly reflective basal zones interpreted as subglacial perchlorate brine pools sustained at temperatures near 240 K, extensive follow-up simulations suggest a more conservative, abiotic alternative [181,189]. Mineralogical and dielectric modeling demonstrates that semi-conducting Noachian clays (Fe/Mg smectites), hydrated saline ice sheets, and flat-lying volcanic basements produce identical high-reflectivity radar echoes under polar pressures without requiring liquid water to remain stable [189].

Topographic effects play a significant role in calibrating these remotely sensed datasets. Intense variations in local terrain angles and solar incidence positions alter surface reflectance profiles, generating severe shadowing along steep scarp faces that can distort automated spectral mapping [190]. Because these layered ice formations provide the most continuous record of recent atmospheric evolution, deciphering their origin remains a top priority for NASA's Mars Exploration Program Analysis Group (MEPAG). Atmospheric models suggest that variations in CO_2 condensation cycles, driven by chaotic obliquity swings or global peak dust storms, regulate the alternating sedimentation rates of dust and ice at the poles [191]. It is widely accepted that the Martian PLDs record the incremental, orbital-scale deposition and removal of water ice and suspended dust, behaving similarly to Milankovitch climate cycles on Earth [192]. This volatile inventory is further backed by cosmochemical data from Martian meteorites. Isotopic studies of hydrous mineral phases, such as apatite and kaersutite amphiboles within SNC samples, provide critical baseline calibrations for the planet's primary volatile budget [176]. Mechanically, the PLDs represent the largest reservoirs of water ice in the inner Solar System outside of Earth [179]. These kilometric-thick formations behave much like terrestrial ice sheets, yet their long-term preservation curves differ fundamentally. Unlike Earth's complex climate, which is regulated by oceans, a global biosphere, and active plate tectonics, Mars' climate system is driven entirely by pure atmospheric and orbital mechanics. This relative simplicity renders Mars an ideal, uncorrupted planetary laboratory for testing the fundamental drivers of global climate change [193].

15. Integration of Multiscale Datasets

As planetary exploration scales across the inner Solar System, autonomous surface rovers accumulate immense, high-density volumes of multi-spectral data that frequently challenge existing data pipelines and downstream analysis capacities. For example, the Mars Exploration Rovers Spirit and Opportunity generated hundreds of thousands of raw and calibrated microscopic images over their multi-year lifetimes, archiving pristine visual snapshots of localized terrain textures [194]. Prospective long-duration surface assets are projected to traverse greater lateral baselines and operate over decadal scales, generating exponentially larger datasets that demand automated processing architectures. Historically, orbital platforms like the Thermal Emission Imaging System (THEMIS) aboard Mars Odyssey and the Mars Orbiter Laser Altimeter (MOLA) aboard Mars Global Surveyor provided the foundational topographies and regional mineral maps needed to contextualize these localized landforms [195].

Simultaneously, deep-trench surface analytical laboratories, such as the Mars Science Laboratory Curiosity rover, continuously track volatile and organic molecule distributions across ancient lakebeds, providing the high-fidelity chemical baselines required to model biosignature preservation potential [94]. On Earth, interpreting comparable high-resolution remote sensing imagery requires advanced processing techniques like Object-Based Image Analysis (OBIA) to achieve high-precision land-cover classification and automated edge-detection [30]. Applied to Mars, this multiscale integration becomes essential for reconstructing ancient atmospheres. While paleohydrological features document widespread, open-system surface fluid activity, climate simulations must blend these orbital views with surface geochemistries to model how Mars sustained a transiently warm and humid climate rather than existing as a permanently locked, frozen world [124]. Automated software pipelines including the Integrated Software for Imagers and Spectrometers (ISIS) and the Martian Surface Isotope (MarSI) model tools allow researchers to simulate these dynamic paleoclimates, enabling broad morphometric mapping and large-scale 3D visualizations of evolving geomorphic landforms [62].

This multiscale framework has been profoundly updated by subsurface data from NASA's In-Sight lander. Its Seismic Experiment for Interior Structure (SEIS) instrument detected over 1300 distinct marsquakes, demonstrating that the primary crust is stratified and varies in thickness from 24 to 72 km [41]. Early inversions of these seismic velocities suggested an entirely molten metallic core, an interpretation that stood in tension with long-term core-cooling metrics. However, a major paradigm shift was achieved through the advanced processing of delayed, low-frequency seismic wave phases transiting through the deep center [87]. By successfully isolating core-transiting PKKP paths and inner core boundary reflecting PKiKP wave reflections, geophysicists confirmed that Mars actually possesses a solid, crystalline metallic inner core with a radius of approximately 613 ± 67 km, encased within a liquid outer core [87]. Concurrently, the Rotation and Interior Structure Experiment (RISE)

component tracking high-precision Doppler shifts constrained the planet's bulk moment of inertia and rotational precessions. Synthesizing these multi-tiered records proves that while the inner core is actively crystallizing, the resulting compositional convection is thermally trapped by the insulating basal molten silicate layer at the base of the mantle, suppressing the core-mantle heat flux and preventing the resurrection of a global dipolar geodynamo [41,87].

16. Discussion and Evolutionary Synthesis

16.1. Comparative Geology and Habitability Constraints

In the global scientific quest to isolate Earth-like habitable worlds, Mars stands as a vital cornerstone and the primary focal point of modern astrobiological exploration [163]. Preserved geomorphological structures, extensive paleohydrological networks, and records of an ancient, denser atmosphere strongly support the hypothesis that early Mars possessed long-lived surface habitability capable of initiating prebiotic chemical pathways [118,140]. A multi-parametric comparison of the structural, geological, and atmospheric baselines driving both Earth and Mars is mapped comprehensively in Table 2.

Table 2. Quantitative physical, atmospheric, and geodynamic baseline comparison between Earth and Mars.

Comparative Parameter	Terrestrial (Earth) System Baseline	Martian System Baseline
Similarities		
Geomorphology	Complex landforms sculpted by globally active water, ice, and wind dynamics. Extraterrestrial signatures (impact craters) are rapidly erased.	Relic networks of canyons, valleys, deltas, and alluvial fans sculpted by past water/ice systems, alongside globally active modern aeolian features.
Sedimentation	Prolific modern and ancient sedimentary strata preserving climbing ripples, cross-bedding, and deep basin cycles.	Well-preserved ancient sedimentary structures including rhythmic bedding, cross-bedding, and mudstone formations derived from mafic sources.
Primary Rock Types	Balanced distribution of igneous, sedimentary, and metamorphic rock suites driven by dynamic plate recycling.	Dominantly mafic igneous rocks (high-iron basalts); granitic/felsic rocks are highly localized and rare due to a lack of active crustal recycling. Low-grade metamorphic rocks are inferred via orbiters, but high-grade regional metamorphism is completely unrecorded.
Rotation Period	23 h, 56 min, 4 s (Sidereal day).	24 h, 37 min, 22 s (Sidereal day; solar sol runs 24 h 39 m).
Differences		
Orbital Revolution	365.25 days (1.00 Earth Year).	~686.93 days (~1.88 Earth Years).
Equatorial Diameter	~12,756.2 km (1.00 Earth diameterbaseline).	~6792 km (Approximately 53% of Earth's diameter).
Surface Gravity	~9.81 m/s^2 (1.00 g baseline).	~3.73 m/s^2 (Approximately 38% of Earth's gravity).
Atmospheric Pressure	101.3 kPa (1.01 bar at sea level).	~0.6 to 0.7 kPa (Mean of 6.1 mbar; ~1% of Earth's atmospheric density).
Atmospheric Composition	Dense, protective gas shield: 78% N_2, 21% O_2, 0.9% Ar, 0.04% CO_2, alongside trace water vapor and noble gases.	Hyper-attenuated, anoxic gas layer: 95.32% CO_2, 2.7% N_2, 1.6% Ar, 0.13% O_2, 0.08% CO, alongside highly variable O_3 and H_2O.
Dust Suspension Mechanics	Suspended particles are rapidly precipitated out by high gravity and persistent moisture/rain cycles.	Low surface gravity and low atmospheric density allow fine aerosols to remain airborne for extended periods, driving high global Aerosol Optical Depth (AOD).
Tropopause Boundary	Distinct tropopause present, acting as a rigid thermodynamic barrier that prevents dust storms from entering the stratosphere.	Tropopause boundary is functionally absent, permitting local dust plumes to loft unhindered into the upper atmosphere.

Table 2. *Cont.*

Comparative Parameter	Terrestrial (Earth) System Baseline	Martian System Baseline
Differences		
Global Magnetic Field	Present; robust geodynamo projects a core-driven dipolar shield protecting the atmosphere from solar stripping.	Absent; global dynamo ceased ~3.5 to 3.9 Ga. Retains intense, asymmetric crustal remanent patches across the ancient southern highlands.
Solar Absorbance	Atmosphere directly absorbs ~23% of incident solar radiation, driving a robust greenhouse effect.	Gaseous envelope absorbs <1% of incident solar light, limiting the greenhouse warming potential to a nominal ~5 K.
Orbital Obliquity	Stabilized by a massive natural satellite; narrow oscillations between 22.1° and 24.5° generate stable seasonal cycles.	Unstabilized and highly chaotic; shifts dynamically from 0° to nearly 60°, driving massive polar cap ice sublimation and catastrophic paleofloods.
Mean Temperature	~15 °C (59 °F); well-buffered by dense ocean-atmosphere thermal cycles.	~−65 °C (−85 °F); hyper-arid baseline subject to extreme diurnal swings due to low thermal inertia.
Thermal Equator Profile	Highly dynamic; ranges from 25.85 °C to 34.75 °C across equatorial belts, heavily distorted by ocean currents.	Structurally simplified and parallel to the equator; exhibits localized, bimodal branches (10° N and 20° S) due to a lack of marine buffers.
Natural Satellites	Single massive moon (Luna; distance ~384,400 km) that actively anchors Earth's spin axis and drives oceanic tides.	Two minor capture-asteroids (Phobos and Deimos). Phobos orbits hyper-close (~6000 km) with negligible mass (1/1000th Earth gravity equivalent), exerting minimal gravitational torque.
Geodynamic Regime	Active mobile-lid plate tectonics, driving widespread orogeny, subduction zones, and dynamic recycling.	Stagnant-lid geodynamic tectonics. Subduction is impossible because iron-rich Martian basalts cannot convert into high-density eclogite phase-changes necessary to achieve negative slab buoyancy. Lithospheric thickening over time generated a rigid single-plate structure that transfers internal heat strictly via conduction.

Integrating these comparative datasets demonstrates that geological factors, such as broad geomorphological features, active intra-crater sedimentation, primary mafic rock types, and an almost identical diurnal rotation period show striking parallels to Earth. Conversely, several fundamental parameters vary drastically from the terrestrial standard. Modern Mars is defined by an anoxic, CO_2-dominated atmosphere, intense surface ultraviolet (UV) radiation, freezing global temperatures, and negligible surface water activity [196,197]. This baseline is further complicated by episodic orbital factors, including chaotic obliquity swings, and localized constraints such as extreme regolith hypersalinity, highly acidic soils, poor redox potentials (Eh) within lingering brines, the pervasive accumulation of toxic perchlorates, and unhindered solar particle events or galactic cosmic rays [198].

Collectively, these findings lead to the definitive assertion that while Mars cannot be scientifically validated as Earth's planetary twin, it can be accurately classified as Earth's distant "geological cousin". This relationship offers an invaluable evolutionary contrast that helps clarify the unique requirements of Earth's long-term biospheric stability [77]. Asserting Mars as an identical twin is a major challenge; its hyper-arid, unbreathable modern environment represents a lethal, frozen desert [197]. Lacking a dense ozone layer, the hyper-attenuated atmosphere permits an intense flux of incident solar UV radiation to reach the surface, actively breaking down organic molecules and creating a highly sterilized surficial boundary layer [199]. Furthermore, the near-absence of complementary trace greenhouse gases restricts thermal infrared trapping to a nominal 20%, maintaining global temperatures far below the terrestrial baseline [196].

16.2. Constraints on the Stagnant-Lid Core-Mantle

Designating Mars as a stagnant-lid 'geological cousin' rather than a mobile-lid 'planetary twin' is governed by a fundamental planetary threshold, viz. the total mass of the world dictates its internal cooling rate [39,77]. On

Earth, vigorous mantle convection drives lateral plate motion and crustal recycling. This active 'mobile-lid' geodynamic engine functions as a global thermochemical thermostat, continuously recycling carbon and water between the surface and the deep interior to stabilize the long-term climate over billions of years [77,78] (Refer to Figure 5). Conversely, because Mars possesses only ~11% of Earth's bulk mass, its primary heat inventory dissipated rapidly. This accelerated thermal decline forced the outer lithosphere to freeze into a single, immobile planetary shell, establishing a permanent 'stagnant-lid' geodynamic regime [82,200] (Refer to Comparative Figure 7).

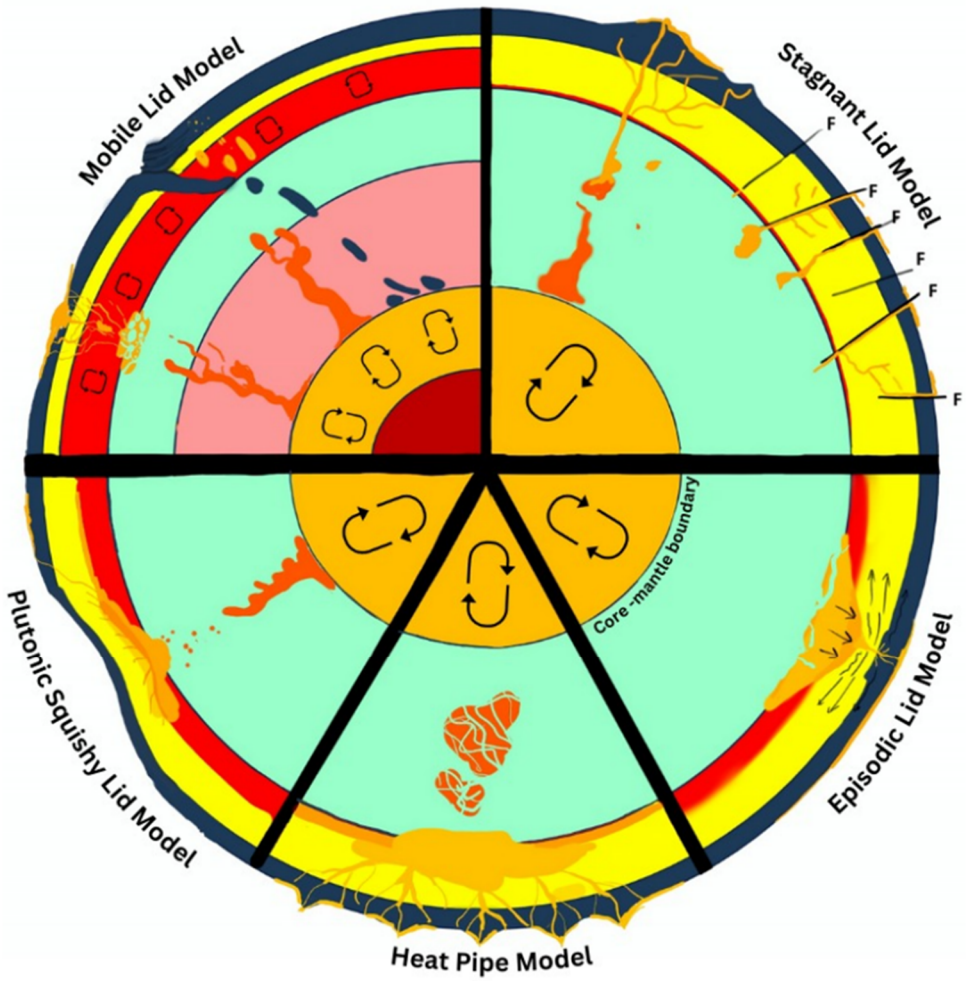

Figure 7. Comparison between mobile lid, stagnant lid and episodic lid models (modified after [77,200–203]).

Due to the iron-rich nature of the Martian mantle, ascending partial melts generated high-density basalts that were mineralogically incapable of achieving the buoyancy thresholds required to trigger subduction [178,198]. Lacking crustal recycling pathways, Mars became geophysically trapped. Its iron-rich volcanic crust functioned as an immutable chemical sponge, permanently absorbing early water budgets into secondary hydrous mineral assemblages via widespread crustal serpentinization [178]. Simultaneously, because the crust remained completely static, deep-seated mantle plumes remained locked beneath fixed volcanic hotspots like the Tharsis province for billions of years [104].

The contrasting tectonic regimes of Earth and Mars provide an important context for understanding their divergent evolutionary histories. On Earth, mobile-lid tectonics facilitates crustal recycling and contributes to the exchange of volatile elements between the surface and interior [86,87]. Mars, by contrast, is characterized predominantly by a stagnant-lid regime, which limits global crustal recycling. Differences in planetary size, interior thermal evolution, and tectonic behaviour may have influenced the evolution of the Martian interior and magnetic field, with implications for atmospheric evolution and surface habitability [86,87]. However, these processes are interconnected, and their relative contributions to the divergent histories of Earth and Mars remain subjects of scientific investigation. Therefore, this comparison brings to fore the importance of considering multiple geological and geophysical factors when evaluating planetary evolution and long-term habitability, rather than attributing these outcomes to a single universal rule.

16.3. Engineering Scenarios and Terraforming Limits

To address these environmental constraints, planetary engineers have modeled speculative terraforming mechanisms designed to artificially raise Martian surface temperatures [204]. Early theoretical configurations proposed introducing large quantities of volatile greenhouse gases or redirecting ammonia-rich icy asteroids toward the planet [204]. While importing massive volatile volumes remains technologically unfeasible, releasing artificial, high-efficiency greenhouse compounds such as perfluorocarbons (PFCs) directly from localized crustal materials could trap upwelling thermal radiation and initiate a gradual warming loop [205]. However, executing this approach requires industrial-scale fluorine mining across the Martian crust that matches or exceeds current terrestrial extraction metrics, posing monumental logistical and engineering challenges [205].

Alternative proposals evaluate using Sun-synchronous orbital solar reflectors massive space-bound mirrors designed to artificially increase polar solar insolation [206]. This method aims to sublimate the frozen CO_2 polar caps to thicken the atmosphere, an approach that has been extended to include controversial proposals for controlled subsurface nuclear detonations to accelerate volatile release [206]. However, milestone climate models published by Jakosky and Edwards (2018) have severely constrained these scenarios. Their work proves that Mars simply does not possess enough hidden, accessible CO_2 reservoirs within its modern polar ice or regolith to achieve a scientifically meaningful greenhouse warming loop, meaning that modern terraforming concepts remain entirely beyond current technological capabilities [177].

This atmospheric inflation limit is permanently exacerbated by the lack of a protective magnetic shield. Unshielded solar wind interactions continuously strip volatile components away into space via induced magnetic pileup and ionospheric mass loading [43,44]. Although the ancient southern crust preserves localized remanent magnetic patches, these are entirely insufficient to support large-scale atmospheric retention [45]. To circumvent this planetary loss, engineering concepts propose creating an artificial magnetic field by generating a high-velocity, charged particle ring along the orbit of Phobos [207]. Concurrently, localized electromagnetic shields could be induced around landed infrastructure to simulate Earth's protective magnetosphere, establishing localized radiation sanctuaries for surface habitats [208].

16.4. Microbial Introduction and Survival in the Martian Subsurface

On a biological level, initiating controlled ecological processes via microbial introduction represents a primary step toward future biosphere stabilization [209]. Identifying specialized microbes exhibiting extreme biodegradable, bioremedial, hypopiezophilic, and radiation-tolerant properties remains central to ecological planning [164]. Advanced environmental simulation testing demonstrates that the photosynthetic cyanobacterium *Nostoc commune* represents an exceptional candidate for survival, capable of exploiting salt deliquescence within hyper-saline brines to sustain metabolic activity and synthesize complex organic matrices [210]. Next-generation genetic engineering could tailor synthetic extremophiles to withstand surface perchlorates and radiation regimes [67].

However, because the surface environment remains highly hostile, the deep Martian subsurface is universally recognized as the most promising location for initial colonization and astrobiological preservation [211]. Within these deep layers, localized volcanic outgassing and relict hydrothermal networks may continue to drive the synthesis of complex organic macromolecules [212]. Ultimately, by mapping extreme terrestrial environments from deep-sea hydrothermal vents to hyper-arid subglacial channels, planetary science builds the multi-disciplinary templates needed to understand Mars' deep interior, evaluate its past habitability, and map out the ultimate future of human expansion across the inner Solar System [213].

17. Conclusions

While Mars remains widely popularized as Earth's twin due to striking physical parallels including near-identical diurnal rotational rates, stable axial tilts, and an extensive historical archive of surface liquid water, this traditional comparative paradigm completely collapses under rigorous geological, atmospheric, and geophysical scrutiny. Mars fundamentally lacks the mobile-lid plate tectonics, sustained core geodynamo, and buffered climate systems that govern Earth's long-term biospheric habitability. Its modern hyper-attenuated, CO_2-dominated atmosphere, highly chaotic orbital obliquity cycles, and complete lack of a global dipolar magnetic shield expose its sub-aerial boundary layer to sterilizing cosmic radiation while permanently restricting the thermodynamic stability of liquid surface water.

Although extensive geomorphological and mineralogical datasets track a warmer, dynamically active early history characterized by branching valley networks, prograding deltas, and clay-rich lacustrine beds, these open-system environments were transient and episodic. The long-term habitable zones on Mars were overwhelmingly subsurface, chemically closed, and hydrothermally driven. Furthermore, the planet's primary evolutionary

trajectory diverged early in its history due to its smaller planetary mass and rapid internal cooling. This accelerated thermal decline caused early atmospheric stripping into space, while its iron-rich, FeO-enriched lavas acted as an immutable geochemical sponge, trapping a vast water inventory directly inside metamorphic minerals within the deep crust.

Recent deep seismic mapping confirms that while Mars has entered its core crystallization epoch, developing a distinct solid inner core, this interior engine remains thermally insulated by a thick layer of basal molten silicates, permanently preventing the resurrection of a global magnetic field. Ultimately, despite compelling terrestrial process-analogues and brief, ancient prebiotic windows, Mars cannot be scientifically validated as a true planetary twin to Earth. Instead, it represents a distinct evolutionary cousin a stagnant-lid terrestrial system that followed a radically divergent, hyper-arid, and hostile path, offering a powerful cosmic baseline to evaluate the unique requirements of Earth's long-term environmental stability.

Author Contributions

K.J.: Conceptualization, Methodology, Investigation, Writing—original draft preparation; K.R.: Supervision, Writing—review and editing; P.G.: Writing—review and editing; K.D.: Writing—review and editing; T.N.: Literature review, Investigation; S.J.: Writing—review and editing; M.L.D.: Writing—review and editing; M.S.: Writing—review and editing. All authors have read and agreed to the published version of the manuscript. The author contributions are described in accordance with the Contributor Roles Taxonomy.

Funding

This research received no external funding.

Institutional Review Board Statement

Not applicable.

Informed Consent Statement

Not applicable.

Data Availability Statement

No new data were generated in this study.

Acknowledgments

The authors acknowledge NASA/JPL-Caltech/University of Arizona, NASA/JPL-Caltech/Malin Space Science Systems (MSSS), and NASA/JPL/GSFC for the Mars exploration imagery utilized in this article. The authors also acknowledge the NASA Planetary Data System (PDS) for providing open access to the Mars Science Laboratory (MSL) Alpha Particle X-ray Spectrometer (APXS) datasets. ESA/DLR/FU-Berlin is formally acknowledged for the image of Jezero Crater captured by the Mars Express HRSC instrument team.

Conflicts of Interest

Given the role as Associate Editor of ESP, Kirtikumar Randive had no involvement in the peer review of this paper and had no access to information regarding its peer-review process. Full responsibility for the editorial process of this paper was delegated to another editor of the journal.

Use of AI and AI-Assisted Technologies

During the preparation of this manuscript, the authors used AI-assisted tool Grammarly for grammatical polishing, line-by-line language editing, and numerical citation formatting. The underlying scientific ideas, data synthesis, literature evaluation, and scientific conclusions are entirely the original work of the authors. After using this tool, the authors reviewed and edited the content as needed and take full responsibility for the content of the published article.

References

1. Taylor, S.R. *Solar System Evolution: A New Perspective*; Cambridge University Press: Cambridge, UK, 2001.
2. Mangold, N.; Baratoux, D.; Witasse, O.; et al. Mars: A small terrestrial planet. *Astron. Astrophys. Rev.* **2016**, *24*, 15. https://doi.org/10.1007/s00159-016-0099-5.
3. Grant, J.A.; Irwin, R.P., III; Grotzinger, J.P.; et al. HiRISE imaging of impact megabreccia and sub-meter aqueous strata in Holden Crater, Mars. *Geology* **2008**, *36*, 195–198. https://doi.org/10.1130/g24340a.1.
4. Lakdawalla, E. Why Is Only Half of Mars Magnetized? The Planetary Society. 2008. Available online: https://www.planetary.org/articles/1710 (accessed on 16 September 2024).
5. Murphy, J.; Steakley, K.; Balme, M.; et al. Field Measurements of Terrestrial and Martian Dust Devils. *Space Sci. Rev.* **2016**, *203*, 39–87. https://doi.org/10.1007/s11214-016-0283-y.
6. Grau Galofre, A.; Jellinek, A.M.; Osinski, G.R. Valley formation on early Mars by subglacial and fluvial erosion. *Nat. Geosci.* **2020**, *13*, 663–668. https://doi.org/10.1038/s41561-020-0618-x.
7. Joseph, R.; Armstrong, R.A.; Duvall, D. Spiders on Mars: Gale crater, cyanobacteria, stromatolites, fungus, mineral-soil concretions. *J. Cosmol.* **2022**, *31*, 44–74.
8. Kumar, P.S.; Kring, D.A. Impact fracturing and structural modification of sedimentary rocks at Meteor Crater, Arizona. *J. Geophys. Res. Planets* **2008**, *113*, E09009. https://doi.org/10.1029/2008je003115.
9. Cockell, C.S.; Bush, T.; Bryce, C.; et al. Habitability: A Review. *Astrobiology* **2016**, *16*, 89–117. https://doi.org/10.1089/ast.2015.1295.
10. Haider, S.A. Introduction. In *Aeronomy of Mars*; Springer Nature: Singapore, 2023. https://doi.org/10.1007/978-981-99-3138-5_1.
11. Savijärvi, H.; Crisp, D.; Harri, A.M. Effects of CO_2 and dust on present-day solar radiation and climate on Mars. *Q. J. R. Meteorol. Soc.* **2005**, *131*, 2907–2922. https://doi.org/10.1256/qj.04.09.
12. Pierrehumbert, R.T. *Principles of Planetary Climate*; Cambridge University Press: Cambridge, UK, 2010. https://doi.org/10.1017/cbo9780511780783.
13. Turbet, M.; Tran, H.; Pirali, O.; et al. Far infrared measurements of absorptions by CH_4 + CO_2 and H_2 + CO_2 mixtures and implications for greenhouse warming on early Mars. *Icarus*. **2018**, *321*, 189–199. https://doi.org/10.1016/j.icarus.2018.11.021.
14. Read, P.L.; Lewis, S.R.; Mulholland, D.P. The physics of Martian weather and climate: A review. *Rep. Prog. Phys.* **2015**, *78*, 125901. https://doi.org/10.1088/0034-4885/78/12/125901.
15. López-Cayuela, M.Á.; Zorzano, M.P.; Guerrero-Rascado, J.L.; et al. Quantitative analysis of the Martian atmospheric dust cycle: Transported mass, surface dust lifting and sedimentation rates. *Icarus* **2024**, *409*, 115854. https://doi.org/10.1016/j.icarus.2023.115854.
16. Mischna, M.A.; Piqueux, S. The role of atmospheric pressure on Mars surface properties and early Mars climate modeling. *Icarus* **2020**, *342*, 113496. https://doi.org/10.1016/j.icarus.2019.113496.
17. Hartwick, V.L.; Haberle, R.M.; Kahre, M.A.; et al. The Dust Cycle on Mars at Different Orbital Distances from the Sun: An Investigation of the Impact of Radiatively Active Dust on Land Planet Climate. *Astrophys. J.* **2022**, *941*, 54. https://doi.org/10.3847/1538-4357/ac9481.
18. Madeleine, J.B.; Forget, F.; Millour, E.; et al. The influence of radiatively active water ice clouds on the Martian climate. *Geophys. Res. Lett.* **2012**, *39*, L23202. https://doi.org/10.1029/2012gl053564.
19. Caillé, V., Spiga, A., Määttänen, A.; et al. Resolving Convection of CO_2 Ice Clouds in the Martian Polar Nights. *Geophys. Res. Lett.* **2024**, *51*, e2023GL106923. https://doi.org/10.1029/2023GL106923.
20. Pettengill, G.H.; Ford, P.G. Winter clouds over the North Martian Polar Cap. *Geophys. Res. Lett.* **2000**, *27*, 609–612. https://doi.org/10.1029/1999gl010896.
21. Chao, B.F.; Rubincam, D.P. Variations of Mars gravitational field and rotation due to seasonal CO_2 exchange. *J. Geophys. Res. Solid Earth* **1990**, *95*, 14755–14760. https://doi.org/10.1029/jb095ib09p14755.
22. Oberst, J.; Wickhusen, K.; Gwinner, K.; et al. Planetary polar explorer—The case for a next-generation remote sensing mission to low Mars orbit. *Exp. Astron.* **2022**, *54*, 695–711. https://doi.org/10.1007/s10686-021-09820-x.
23. McCleese, D.J.; Heavens, N.G.; Schofield, J.T.; et al. Structure and dynamics of the Martian lower and middle atmosphere as observed by the Mars Climate Sounder: Seasonal variations in zonal mean temperature, dust, and water ice aerosols. *J. Geophys. Res. Planets* **2010**, *115*, E12016. https://doi.org/10.1029/2010je003677.
24. Head, J.W.; Mustard, J.F.; Kreslavsky, M.A.; et al. Recent ice ages on Mars. *Nature* **2003**, *426*, 797–802. https://doi.org/10.1038/nature02114.
25. Laskar, J.; Correia, A.C.M.; Gastineau, M.; et al. Long term evolution and chaotic diffusion of the insolation quantities of Mars. *Icarus* **2004**, *170*, 343–364. https://doi.org/10.1016/j.icarus.2004.04.005.
26. Greeley, R.; Balme, M.R.; Iversen, J.D.; et al. Martian dust devils: Laboratory simulations of particle threshold. *J. Geophys. Res. Planets* **2003**, *108*, 5041. https://doi.org/10.1029/2002je001987.

27. Newman, C.E.; Kahanpää, H.; Richardson, M.I.; et al. MarsWRF Convective Vortex and Dust Devil Predictions for Gale Crater over 3 Mars Years and Comparison With MSL-REMS Observations. *J. Geophys. Res. Planets* **2019**, *124*, 3442–3468. https://doi.org/10.1029/2019je006082.
28. Wang, Y.; Li, B.; Zhang, J.; et al. The Preliminary Study of Dust Devil Tracks in Southern Utopia Planitia, Landing Area of Tianwen-1 Mission. *Remote Sens.* **2021**, *13*, 2601. https://doi.org/10.3390/rs13132601.
29. Fisher, J.A.; Richardson, M.I.; Newman, C.E.; et al. A survey of Martian dust devil activity using Mars Global Surveyor Mars Orbiter Camera images. *J. Geophys. Res. Planets* **2005**, *110*, E03004. https://doi.org/10.1029/2003je002165.
30. He, F.; Rong, Z.; Wu, Z.; et al. Martian Dust Storms: Reviews and Perspective for the Tianwen-3 Mars Sample Return Mission. *Remote Sens.* **2024**, *16*, 2613. https://doi.org/10.3390/rs16142613.
31. Chapman, R.M.; Lewis, S.R.; Balme, M.; et al. Diurnal variation in martian dust devil activity. *Icarus* **2017**, *292*, 154–167. https://doi.org/10.1016/j.icarus.2017.01.003.
32. Balme, M.; Greeley, R. Dust devils on Earth and Mars. *Rev. Geophys.* **2006**, *44*, RG3003. https://doi.org/10.1029/2005rg000188.
33. Suman, A.; Zanini, N. Erosion assessment with Martian dust. *Acta Astronaut.* **2024**, *214*, 380–388. https://doi.org/10.1016/j.actaastro.2023.10.034.
34. Murdoch, N.; Stott, A.E.; Gillier, M.; et al. The sound of a Martian dust devil. *Nat. Commun.* **2022**, *13*, 7505. https://doi.org/10.1038/s41467-022-35100-z.
35. Mars Global Surveyor. Magnetic Field Experiment MAG/ER. NASA. 2017. Available online: https://mgs-mager.gsfc.nasa.gov/ (accessed on 21 September 2026).
36. Balogh, A. Planetary Magnetic Field Measurements: Missions and Instrumentation. *Space Sci. Rev.* **2010**, *152*, 23–97. https://doi.org/10.1007/s11214-010-9643-1.
37. Dolginov, S.S. The magnetic field and the magnetosphere of the planet Mars. *Adv. Space Res.* **1992**, *12*, 187–211. https://doi.org/10.1016/0273-1177(92)90279-x.
38. Savitsky, Z. Mars's magnetic field was long-lived, reversible. *Science* **2022**, *378*, 1262–1263. https://doi.org/10.1126/science.adg3931.
39. Samuel, H.; Drilleau, M.; Rivoldini, A.; et al. Geophysical evidence for an enriched molten silicate layer above Mars's core. *Nature* **2023**, *622*, 712–717. https://doi.org/10.1038/s41586-023-06601-8. Correction in *Nature* **2024**, *625*, E13.
40. Hemingway, D.J.; Driscoll, P.E. History and Future of the Martian Dynamo and Implications of a Hypothetical Solid Inner Core. *J. Geophys. Res. Planets* **2021**, *126*, e2020JE006663. https://doi.org/10.1029/2020je006663.
41. Khan, A.; Huang, D.; Durán, C.; et al. Evidence for a liquid silicate layer atop the Martian core. *Nature* **2023**, *622*, 718–723. https://doi.org/10.1038/s41586-023-06586-4.
42. Arkani-Hamed, J.; Boutin, D. Paleomagnetic poles of Mars: Revisited. *J. Geophys. Res. Planets* **2004**, *109*, E03011. https://doi.org/10.1029/2003je002229.
43. Halekas, J.S.; Ruhunusiri, S.; Harada, Y.; et al. Structure, dynamics, and seasonal variability of the Mars-solar wind interaction: MAVEN Solar Wind Ion Analyzer in-flight performance and science results. *J. Geophys. Res. Space Phys.* **2017**, *122*, 547–578. https://doi.org/10.1002/2016ja023167.
44. Vaisberg, O.L.; Ermakov, V.N.; Shuvalov, S.D.; et al. The Structure of Martian Magnetosphere at the Dayside Terminator Region as Observed on MAVEN Spacecraft. *J. Geophys. Res. Space Phys.* **2018**, *123*, 2679–2695. https://doi.org/10.1002/2018ja025202.
45. Lillis, R.J.; Robbins, S.; Manga, M.; et al. Time history of the Martian dynamo from crater magnetic field analysis. *J. Geophys. Res. Planets* **2013**, *118*, 1488–1511. https://doi.org/10.1002/jgre.20105.
46. Gooding, J.L. Chemical weathering on Mars thermodynamic stabilities of primary minerals (and their alteration products) from mafic igneous rocks. *Icarus* **1978**, *33*, 483–513. https://doi.org/10.1016/0019-1035(78)90186-0.
47. Bridges, J.C.; Catling, D.C.; Saxton, J.M.; et al. Alteration Assemblages in Martian Meteorites: Implications for Near-Surface Processes. *Space Sci. Rev.* **2001**, *96*, 365–392. https://doi.org/10.1023/a:1011965826553.
48. Rao, M.N.; Borg, L.E.; McKay, D.S.; et al. Martian soil component in impact glasses in a Martian meteorite. *Geophys. Res. Lett.* **1999**, *26*, 3265–3268. https://doi.org/10.1029/1999gl005388.
49. Bogard, D.D.; Johnson, P. Martian Gases in an Antarctic Meteorite? *Science* **1983**, *221*, 651–654. https://doi.org/10.1126/science.221.4611.651.
50. Becker, R.H.; Pepin, R.O. The case for a martian origin of the shergottites: Nitrogen and noble gases in EETA 79001. *Earth Planet. Sci. Lett.* **1984**, *69*, 225–242. https://doi.org/10.1016/0012-821x(84)90183-3.
51. Condie, K.C. Comparative Planetary Evolution. In *Earth as an Evolving Planetary System*, 2nd ed.; Elsevier: Cambridge, MA, USA, 2011; pp. 437–492. https://doi.org/10.1016/b978-0-12-385227-4.00001-8.
52. Borg, L.E.; Nyquist, L.E.; Taylor, L.A.; et al. Constraints on Martian differentiation processes from Rb-Sr and Sm-Nd isotopic analyses of the basaltic shergottite QUE 94201. *Geochim. Cosmochim. Acta* **1997**, *61*, 4915–4931. https://doi.org/10.1016/s0016-7037(97)00276-7.

53. Nyquist, L.E.; Bogard, D.D.; Shih, C.Y.; et al. Ages and Geologic Histories of Martian Meteorites. *Space Sci. Rev.* **2001**, *96*, 105–164. https://doi.org/10.1023/a:1011993105172.
54. Sheen, A.I.; Herd, C.D.K.; Staddon, L.; et al. Baddeleyite microstructural response to shock metamorphism in three enriched shergottites and implications for U–Pb geochronology. *Geochim. Cosmochim. Acta* **2024**, *366*, 267–283. https://doi.org/10.1016/j.gca.2023.12.002. Correction in *Geochim. Cosmochim. Acta* **2024**, *382*, 160.
55. Jennings, E.S.; Coull, P. Olivine microstructure and thermometry in olivine-phyric shergottites Sayh al Uhaymir 005 and Dar al Gani 476. *Meteorit. Planet. Sci.* **2024**, *59*, 55–67. https://doi.org/10.1111/maps.14106.
56. Treiman, A.H. Invited Review: The Nakhlite Meteorites: Augite-Rich Igneous Rocks from Mars. *Chem. Erde* **2005**, *65*, 203–270. https://doi.org/10.1016/j.chemer.2005.01.004.
57. Misawa, K.; Kojima, K.; Imae, N.; et al. The Yamato nakhlite consortium. *Antarct. Meteor. Res.* **2003**, *16*, 1–12. https://doi.org/10.15094/00006023.
58. Beck, P.; Barrat, J.A.; Gillet, P.; et al. Petrography and geochemistry of the chassignite Northwest Africa 2737 (NWA 2737). *Geochim. Cosmochim. Acta* **2006**, *70*, 2127–2139. https://doi.org/10.1016/j.gca.2006.01.016.
59. Treiman, A.H.; Dyar, M.D.; McCanta, M.; et al. Martian Dunite NWA 2737: Petrographic constraints on geological history, shock events, and olivine color. *J. Geophys. Res. Planets* **2007**, *112*, E04002. https://doi.org/10.1029/2006je002777.
60. Krot, A.N.; Keil, K.; Scott, E.R.D.; et al. Classification of Meteorites and Their Genetic Relationships. In *Treatise on Geochemistry*, 2nd ed.; Elsevier: Oxford, UK, 2014; pp. 1–63. https://doi.org/10.1016/b978-0-08-095975-7.00102-9.
61. McSween, H.Y. Petrology on Mars. *Am. Mineral.* **2015**, *100*, 2380–2395. https://doi.org/10.2138/am-2015-5257.
62. Chavan, A.; Sarkar, S.; Thakkar, A.; et al. A New Method of Mosaicking Context Camera (CTX) Images for the Geomorphological Study of Martian Landscape. *Open J. Geol.* **2021**, *11*, 373–380. https://doi.org/10.4236/ojg.2021.118020.
63. Nimmo, F.; Tanaka, K. Early crustal evolution of Mars. *Annu. Rev. Earth Planet. Sci.* **2005**, *33*, 133–161. https://doi.org/10.1146/annurev.earth.33.092203.122637.
64. Christensen, P.R.; McSween, H.Y.; Bandfield, J.L.; et al. Evidence for magmatic evolution and diversity on Mars from infrared observations. *Nature* **2005**, *436*, 504–509. https://doi.org/10.1038/nature03639. Erratum in *Nature* **2005**, *436*, 882.
65. Ahrens, C.; Leone, G. Petrologic evolution of Martian volcanism and clues from meteorites. *Planet. Space Sci.* **2021**, *198*, 105154.
66. NASA Planetary Data System—MSL APXS Datasets. 2025. Available online: https://pds-geosciences.wustl.edu/msl/msl-m-apxs-4_5-rdr-v1/mslapx_1xxx/data/ (accessed on 10 April 2025).
67. Billi, D.; Baqué, M.; Smith, H.; et al. Cyanobacteria from Extreme Deserts to Space. *Adv. Microbiol.* **2013**, *3*, 80–86. https://doi.org/10.4236/aim.2013.36A010.
68. Stolper, E.M.; Baker, M.B.; Newcombe, M.E.; et al. The Petrochemistry of Jake_M: A Martian Mugearite. *Science* **2013**, *341*, 1239463. https://doi.org/10.1126/science.1239463.
69. Sautter, V.; Fabre, C.; Forni, O.; et al. Igneous mineralogy at Bradbury Rise: The first ChemCam campaign at Gale crater. *J. Geophys. Res. Planets* **2014**, *119*, 30–46. https://doi.org/10.1002/2013je004472.
70. McSween, H.Y.; Ruff, S.W.; Morris, R.V.; et al. Alkaline volcanic rocks from the Columbia Hills, Gusev crater, Mars. *J. Geophys. Res. Planets* **2006**, *111*, E09S91. https://doi.org/10.1029/2006je002698.
71. Seelos, F.P.; Seelos, K.D.; Murchie, S.L.; et al. The CRISM investigation in Mars orbit: Overview, history, and delivered data products. *Icarus* **2024**, *419*, 115612. https://doi.org/10.1016/j.icarus.2023.115612.
72. Popa, C.; Esposito, F.; Mennella, V.; et al. Occurrence of anorthosite on Mars in Xanthe Terra. In Proceedings of the European Planetary Science Congress, Rome, Italy, 19–24 September 2010; Volume 5.
73. Carter, J.; Poulet, F. Ancient plutonic processes on Mars inferred from the detection of possible anorthositic terrains. *Nat. Geosci.* **2013**, *6*, 1008–1012. https://doi.org/10.1038/ngeo1995.
74. Werner, S.C. The global martian volcanic evolutionary history. *Icarus* **2009**, *201*, 44–68. https://doi.org/10.1016/j.icarus.2008.12.019.
75. Baratoux, D.; Toplis, M.J.; Monnereau, M.; et al. Thermal history of Mars inferred from orbital geochemistry of volcanic provinces. *Nature* **2011**, *472*, 338–341. https://doi.org/10.1038/nature09903. Erratum in *Nature* **2011**, *475*, 254.
76. Bouvier, A.; Blichert-Toft, J.; Albarède, F. Martian meteorite chronology and the evolution of the interior of Mars. *Earth Planet. Sci. Lett.* **2009**, *280*, 285–295. https://doi.org/10.1016/j.epsl.2009.01.042.
77. Palin, R.M.; Santosh, M. Plate tectonics: What, where, why, and when? *Gondwana Res.* **2021**, *100*, 3–24. https://doi.org/10.1016/j.gr.2020.11.001.
78. Palin, R.; Wade, J.; Dyck, B. Metamorphism in a wet Martian middle crust: Implications for the failure of plate tectonics on Mars. *Proc. Natl. Acad. Sci. USA* **2024**, *121*, e2416680121. https://doi.org/10.1073/pnas.2416680121.
79. Pathare, A.V.; Paige, D.A.; Turtle, E. Viscous relaxation of craters within the Martian south polar layered deposits. *Icarus* **2005**, *174*, 396–418. https://doi.org/10.1016/j.icarus.2004.10.031.
80. Stewart, S.T.; Ahrens, T.J. Shock properties of H_2O ice. *J. Geophys. Res. Planets* **2005**, *110*, E03005. https://doi.org/10.1029/2004je002305.

81. Turenne, N.; Parkinson, A.; Applin, D.M.; et al. Spectral reflectance properties of minerals exposed to martian surface conditions: Implications for spectroscopy-based mineral detection on Mars. *Planet. Space Sci.* **2022**, *210*, 105377. https://doi.org/10.1016/j.pss.2021.105377.
82. Knapmeyer-Endrun, B.; Panning, M.P.; Bissig, F.; et al. Thickness and structure of the martian crust from InSight seismic data. *Science* **2021**, *373*, 438–443. https://doi.org/10.1126/science.abf8966.
83. Yan, C.; Barik, A.; Stanley, S.; et al. Mars' Hemispheric Magnetic Field from a Full-Sphere Dynamo. *Geophys. Res. Lett.* **2025**, *52*, e2024GL113926. https://doi.org/10.1029/2024gl113926.
84. Khan, A.; Liebske, C.; Rozel, A.B.; et al. Upper mantle structure of Mars from InSight seismic data. *Science* **2021**, *373*, 434–438. https://doi.org/10.1126/science.abf2966.
85. Hauck, S.A.; Margot, J.L.; Solomon, S.C.; et al. The curious case of Mercury's internal structure. *J. Geophys. Res. Planets* **2013**, *118*, 1204–1220. https://doi.org/10.1002/jgre.20091.
86. Hefferan, K.; O'Brien, J. *Earth Materials*; Wiley-Blackwell: Hoboken, NJ, USA, 2010.
87. Smrekar, S.E.; Davaille, A.; Sotin, C. Venus Interior Structure and Dynamics. *Space Sci. Rev.* **2018**, *214*, 88. https://doi.org/10.1007/s11214-018-0518-1.
88. Smrekar, S.E.; Stofan, E.R.; Mueller, N.; et al. Recent hotspot volcanism on Venus from VIRTIS emissivity data. *Sci. Adv.* **2019**, *5*, eaaw5306. https://doi.org/10.1126/sciadv.aaw5306.
89. Wilhelms, D.E.; Squyres, S.W. The martian hemispheric dichotomy may be due to a giant impact. *Nature* **1984**, *309*, 138–140. https://doi.org/10.1038/309138a0.
90. Frey, H.; Schultz, R.A. Large impact basins and the mega-impact origin for the crustal dichotomy on Mars. *Geophys. Res. Lett.* **1988**, *15*, 229–232. https://doi.org/10.1029/gl015i003p00229.
91. Stähler, S.C.; Khan, A.; Banerdt, W.B.; et al. Seismic detection of the martian core. *Science* **2021**, *373*, 443–448. https://doi.org/10.1126/science.abi7730.
92. Bi, H.; Sun, D.; Sun, N.; et al. Seismic detection of a 600-km solid inner core in Mars. *Nature* **2025**, *645*, 67–72. https://doi.org/10.1038/s41586-025-09361-9. Correction in *Nature* **2025**, *648*, E18.
93. Malin, M.C.; Edgett, K.S. Evidence for Persistent Flow and Aqueous Sedimentation on Early Mars. *Science* **2003**, *302*, 1931–1934. https://doi.org/10.1126/science.1090544.
94. Grotzinger, J.P.; Milliken, R.E. The sedimentary rock record of Mars: Distribution, origins, and global stratigraphy. In *Sedimentary Geology of Mars*; SEPM Society for Sedimentary Geology: Tulsa, OK, USA, 2012; pp. 1–48. https://doi.org/10.2110/pec.12.102.0001.
95. McLennan, S.M.; Grotzinger, J.P. The sedimentary rock cycle of Mars. In *The Martian Surface*; Cambridge University Press: Cambridge, UK, 2008; pp. 541–577. https://doi.org/10.1017/cbo9780511536076.025.
96. Grotzinger, J.P.; Arvidson, R.E.; Bell, J.F.; et al. Stratigraphy and sedimentology of a dry to wet eolian depositional system, Burns formation, Meridiani Planum, Mars. *Earth Planet. Sci. Lett.* **2005**, *240*, 11–72. https://doi.org/10.1016/j.epsl.2005.09.039.
97. Quantin, C.; Allemand, P.; Mangold, N.; et al. Fluvial and lacustrine activity on layered deposits in Melas Chasma, Valles Marineris, Mars. *J. Geophys. Res. Planets* **2005**, *110*, E12S19. https://doi.org/10.1029/2005je002440.
98. Hayes, A.G.; Grotzinger, J.P.; Edgar, L.A.; et al. Reconstruction of eolian bed forms and paleocurrents from cross-bedded strata at Victoria Crater, Meridiani Planum, Mars. *J. Geophys. Res. Planets* **2011**, *116*, E00F21. https://doi.org/10.1029/2010je003688.
99. Di Achille, G.; Hynek, B.M. Deltas and valley networks on Mars: Implications for a global hydrosphere. *Nat. Geosci.* **2010**, *3*, 455–458.
100. NASA/JPL-Caltech/Univ. of Arizona. Yardangs in Arsinoes Chaos, Mars. 2015. Available online: https://www.nasa.gov/image-article/yardangs-arsinoes-chaos-mars/ (accessed on 24 September 2026)
101. *NASA/JPL-Caltech/Univ. of Arizona*. Ius Chasma. 2008. Available online: https://www.nasa.gov/image-article/ius-chasma/ (accessed on 21 March 2026).
102. NASA/JPL-Caltech/MSSS. Curiosity Views Rhythmic Rock Layers. 2023. Available online: https://www.jpl.nasa.gov/images/pia25734-curiosity-views-rhythmic-rock-layers/ (accessed on 24 October 2025).
103. ESA/DLR/FU-Berlin. Jezero Crater Delta. Available online: https://www.esa.int/ESA_Multimedia/Images/2021/02/Jezero_Crater_delta (accessed on 24 September 2026).
104. Andrews-Hanna, J.C. The formation of Valles Marineris: 3. Trough formation through super-isostasy, stress, sedimentation, and subsidence. *J. Geophys. Res. Planets* **2012**, *117*, E06002. https://doi.org/10.1029/2012je004059.
105. Hurowitz, J.A.; Fischer, W.W.; Tosca, N.J.; et al. Origin of acidic surface waters and the evolution of atmospheric chemistry on early Mars. *Nat. Geosci.* **2010**, *3*, 323–326. https://doi.org/10.1038/ngeo831.
106. Christensen, P.R.; Bandfield, J.L.; Hamilton, V.E.; et al. Mars Global Surveyor Thermal Emission Spectrometer experiment: Investigation description and surface science results. *J. Geophys. Res. Planets* **2001**, *106*, 23823–23871. https://doi.org/10.1029/2000je001370.

107. Bibring, J.P.; Langevin, Y.; Gendrin, A.; et al. Mars Surface Diversity as Revealed by the OMEGA/Mars Express Observations. *Science* **2005**, *307*, 1576–1581. https://doi.org/10.1126/science.1108806.
108. Gendrin, A.; Mangold, N.; Bibring, J.P.; et al. Sulfates in Martian Layered Terrains: The OMEGA/Mars Express View. *Science* **2005**, *307*, 1587–1591. https://doi.org/10.1126/science.1109087.
109. Poulet, F.; Bibring, J.P.; Mustard, J.F.; et al. Phyllosilicates on Mars and implications for early martian climate. *Nature* **2005**, *438*, 623–627. https://doi.org/10.1038/nature04274.
110. Grotzinger, J.P.; Sumner, D.Y.; Kah, L.C.; et al. A Habitable Fluvio-Lacustrine Environment at Yellowknife Bay, Gale Crater, Mars. *Science* **2014**, *343*, 1242777. https://doi.org/10.1126/science.1242777.
111. Morris, R.V.; Lauer, H.V., Jr.; Lawson, C.A.; et al. Spectral and other physicochemical properties of submicron powders of hematite (α-Fe_2O_3), maghemite (γ-Fe_2O_3), magnetite (Fe_3O_4), goethite (α-FeOOH), and lepidocrocite (γ-FeOOH). *J. Geophys. Res. Solid Earth* **1985**, *90*, 3126–3144.
112. Christensen, P.R.; Bandfield, J.L.; Smith, M.D.; et al. Identification of a basaltic component on the Martian surface from Thermal Emission Spectrometer data. *J. Geophys. Res. Planets* **2000**, *105*, 9609–9621. https://doi.org/10.1029/1999je001127.
113. Ehlmann, B.L.; Mustard, J.F.; Murchie, S.L.; et al. Subsurface water and clay mineral formation during the early history of Mars. *Nature* **2011**, *479*, 53–60. https://doi.org/10.1038/nature10582.
114. Kumari, P.; Soor, S.; Shetty, A.; et al. Mineral classification on Martian surface using CRISM hyperspectral data: A survey. *J. Appl. Remote Sens.* **2023**, *17*, 041501. https://doi.org/10.1117/1.jrs.17.041501.
115. Fornaro, T.; Steele, A.; Brucato, J.R. Catalytic/Protective Properties of Martian Minerals and Implications for Possible Origin of Life on Mars. *Life* **2018**, *8*, 56. https://doi.org/10.3390/life8040056.
116. Shkolyar, S.; Farmer, J.D. Biosignature Preservation Potential in Playa Evaporites: Impacts of Diagenesis and Implications for Mars Exploration. *Astrobiology* **2018**, *18*, 1460–1478. https://doi.org/10.1089/ast.2018.1849.
117. Mancinelli, R.L.; Fahlen, T.F.; Landheim, R.; et al. Brines and evaporites: Analogs for Martian life. *Adv. Space Res.* **2004**, *33*, 1244–1246.
118. Ramirez, R.M.; Craddock, R.A. The geological and climatological case for a warmer and wetter early Mars. *Nat. Geosci.* **2018**, *11*, 230–237. https://doi.org/10.1038/s41561-018-0093-9.
119. Bhartia, R.; Beegle, L.W.; DeFlores, L.; et al. Perseverance's Scanning Habitable Environments with Raman and Luminescence for Organics and Chemicals (SHERLOC) Investigation. *Space Sci. Rev.* **2021**, *217*, 58.
120. Sharma, S.; Roppel, R.D.; Murphy, A.E.; et al. Diverse organic-mineral associations in Jezero crater, Mars. *Nature* **2023**, *619*, 724–732.
121. Morgan, A.M. New maximum constraints on the era of martian valley network formation. *Earth Planet. Sci. Lett.* **2024**, *626*, 118509. https://doi.org/10.1016/j.epsl.2023.118509.
122. Hynek, B.M.; Beach, M.; Hoke, M.R.T. Updated global map of Martian valley networks and implications for climate and hydrologic processes. *J. Geophys. Res. Planets* **2010**, *115*, E09008. https://doi.org/10.1029/2009je003548.
123. Plescia, J.B.; Saunders, R.S. Tectonic history of the Tharsis Region, Mars. *J. Geophys. Res. Solid Earth* **1982**, *87*, 9775–9791. https://doi.org/10.1029/jb087ib12p09775.
124. Barlow, N.G. What we know about Mars from its impact craters. *Geol. Soc. Am. Bull.* **2010**, *122*, 644–657. https://doi.org/10.1130/b30182.1.
125. Carr, M.H. *Water on Mars*; Oxford University Press: Oxford, UK, 1996. https://doi.org/10.1093/oso/9780195099386.001.0001.
126. Cutts, J.A. Nature and origin of layered deposits of the Martian polar regions. *J. Geophys. Res.* **1973**, *78*, 4231–4249. https://doi.org/10.1029/jb078i020p04231.
127. Russell, P.S.; Head, J.W. The martian hydrosphere/cryosphere system: Implications of the absence of hydrologic activity at Lyot crater. *Geophys. Res. Lett.* **2002**, *29*, 1827. https://doi.org/10.1029/2002GL015178.
128. Orosei, R.; Ding, C.; Fa, W.; et al. The Global Search for Liquid Water on Mars from Orbit: Current and Future Perspectives. *Life* **2020**, *10*, 120. https://doi.org/10.3390/life10080120.
129. Fassett, C.I. Analysis of impact crater populations and the geochronology of planetary surfaces in the inner solar system. *J. Geophys. Res. Planets* **2016**, *121*, 1900–1926. https://doi.org/10.1002/2016je005094.
130. Frey, H.V.; Roark, J.H.; Shockey, K.M.; et al. Ancient lowlands on Mars. *Geophys. Res. Lett.* **2002**, *29*, 22-1–22-4. https://doi.org/10.1029/2001gl013832.
131. Squyres, S.W.; Carr, M.H. Geomorphic Evidence for the Distribution of Ground Ice on Mars. *Science* **1986**, *231*, 249–252. https://doi.org/10.1126/science.231.4735.249.
132. Carr, M.H.; Crumpler, L.S.; Cutts, J.A.; et al. Martian impact craters and emplacement of ejecta by surface flow. *J. Geophys. Res.* **1977**, *82*, 4055–4065. https://doi.org/10.1029/js082i028p04055.
133. Lagain, A.; Bouley, S.; Baratoux, D.; et al. Mars Crater Database: A participative project for the classification of the morphological characteristics of large Martian craters. In *Large Meteorite Impacts and Planetary Evolution VI*; Geological Society of America: Boulder, CO, USA, 2021; pp. 629–644. https://doi.org/10.1130/2021.2550(29).

134. Doran, P.T.; Clifford, S.M.; Forman, S.L.; et al. Mars chronology: Assessing techniques for quantifying surficial processes. *Earth-Sci. Rev.* **2004**, *67*, 313–337. https://doi.org/10.1016/j.earscirev.2004.04.001.
135. Carr, M.H.; Head, J.W. Martian surface/near-surface water inventory: Sources, sinks, and changes with time. *Geophys. Res. Lett.* **2015**, *42*, 726–732. https://doi.org/10.1002/2014gl062464.
136. Tanaka, K.L. The stratigraphy of Mars. *J. Geophys. Res. Solid Earth* **1986**, *91*, E139–E158. https://doi.org/10.1029/jb091ib13p0e139.
137. Hartmann, W.K.; Neukum, G. Cratering Chronology and the Evolution of Mars. *Space Sci. Rev.* **2001**, *96*, 165–194. https://doi.org/10.1023/a:1011945222010.
138. Tanaka, K.L.; Isbell, N.K.; Scott, D.H.; et al. The resurfacing history of Mars: A synthesis of digitized, Viking-based geology. In Proceedings of the Lunar and Planetary Science Conference, Houston, TX, USA, 14–18 March 1988; pp. 665–678.
139. Tanaka, K.L.; Scott, D.H.; Greeley, R. Global stratigraphy. In *Mars*; University of Arizona Press: Tucson, AZ, USA, 1992; pp. 345–382. https://doi.org/10.2307/j.ctt207g59v.15.
140. Tanaka, K. Dust and Ice Deposition in the Martian Geologic Record. *Icarus* **2000**, *144*, 254–266. https://doi.org/10.1006/icar.1999.6297.
141. Golombek, M.P.; Grant, J.A.; Crumpler, L.S.; et al. Erosion rates at the Mars Exploration Rover landing sites and long-term climate change on Mars. *J. Geophys. Res. Planets* **2006**, *111*, E12S10. https://doi.org/10.1029/2006je002754.
142. Craddock, R.A.; Maxwell, T.A. Geomorphic evolution of the Martian highlands through ancient fluvial processes. *J. Geophys. Res. Planets* **1993**, *98*, 3453–3468. https://doi.org/10.1029/92je02508.
143. Clifford, S.; Parker, T.J. The Evolution of the Martian Hydrosphere: Implications for the Fate of a Primordial Ocean and the Current State of the Northern Plains. *Icarus* **2001**, *154*, 40–79. https://doi.org/10.1006/icar.2001.6671.
144. Tanaka, K.L.; Carr, M.H.; Skinner, J.A.; et al. Geology of the MER 2003 "Elysium" candidate landing site in southeastern Utopia Planitia, Mars. *J. Geophys. Res. Planets* **2003**, *108*, 8079. https://doi.org/10.1029/2003je002054.
145. Greeley, R.; Spudis, P.D. Volcanism on Mars. *Rev. Geophys.* **1981**, *19*, 13–41. https://doi.org/10.1029/rg019i001p00013.
146. Westall, F.; Foucher, F.; Bost, N.; et al. Biosignatures on Mars: What, Where, and How? Implications for the Search for Martian Life. *Astrobiology* **2015**, *15*. 998–1029. https://doi.org/10.1089/ast.2015.1374.
147. Fawdon, P.; Gupta, S.; Davis, J.M.; et al. The Hypanis Valles delta: The last highstand of a sea on early Mars? *Earth Planet. Sci. Lett.* **2018**, *500*, 225–241. https://doi.org/10.1016/j.epsl.2018.07.040.
148. Pullan, D.; Westall, F.; Hofmann, B.A.; et al. Identification of Morphological Biosignatures in Martian Analogue Field Specimens Using *In Situ* Planetary Instrumentation. *Astrobiology* **2008**, *8*, 119–156. https://doi.org/10.1089/ast.2006.0037.
149. Steiner, M.H.; Hausrath, E.M.; Sun, H.Q. Synthesis of potential phosphate mineral biosignatures under Mars-relevant conditions. In Proceedings of the Lunar and Planetary Science Conference, The Woodlands, TX, USA, 18–22 March 2013; p. 2761.
150. Viennet, J.C.; Bernard, S.; Le Guillou, C.; et al. Experimental clues for detecting biosignatures on Mars. *Geochem. Perspect. Lett.* **2019**, *12*, 28–33. https://doi.org/10.7185/geochemlet.1931.
151. Westall, F.; Hickman-Lewis, K.; Cavalazzi, B.; et al. On biosignatures for Mars. *Int. J. Astrobiol.* **2021**, *20*. 377–393. https://doi.org/10.1017/S1473550421000264.
152. Wickramarathna, S.; Chandrajith, R.; Senaratne, A.; et al. Bacterial influence on the formation of hematite: Implications for Martian dormant life. *Int. J. Astrobiol.* **2021**, *20*, 270–284. https://doi.org/10.1017/s1473550421000124.
153. McMahon, S.; Ivarsson, M.; Wacey, D.; et al. Dubiofossils from a Mars-analogue subsurface palaeoenvironment: The limits of biogenicity criteria. *Geobiology* **2021**, *19*, 473–488. https://doi.org/10.1111/gbi.12445.
154. McMahon, S.; Cosmidis, J. False biosignatures on Mars: anticipating ambiguity. *J. Geol. Soc.* **2021**, *179*, jgs2021-050. https://doi.org/10.1144/jgs2021-050.
155. Chan, M.A.; Hinman, N.W.; Potter-McIntyre, S.L.; et al. Deciphering Biosignatures in Planetary Contexts. *Astrobiology* **2019**, *19*, 1075–1102. https://doi.org/10.1089/ast.2018.1903.
156. Summons, R.E.; Amend, J.P.; Bish, D.; et al. Preservation of Martian Organic and Environmental Records: Final Report of the Mars Biosignature Working Group. *Astrobiology* **2011**, *11*, 157–181. https://doi.org/10.1089/ast.2010.0506.
157. Davila, A.F.; Fairén, A.G.; Schulze-Makuch, D.; et al. The ALH84001 Case for Life on Mars. In *From Fossils to Astrobiology*; Springer: Dordrecht, The Netherlands, 2009; pp. 471–489. https://doi.org/10.1007/978-1-4020-8837-7_24.
158. Thomas-Keprta, K.L.; Clemett, S.J.; Bazylinski, D.A.; et al. Magnetofossils from Ancient Mars: A Robust Biosignature in the Martian Meteorite ALH84001. *Appl. Environ. Microbiol.* **2002**, *68*, 3663–3672. https://doi.org/10.1128/aem.68.8.3663-3672.2002.
159. Schmitt-Kopplin, P.; Matzka, M.; Ruf, A.; et al. Complex carbonaceous matter in Tissint martian meteorites give insights into the diversity of organic geochemistry on Mars. *Sci. Adv.* **2023**, *9*, eadd6439. https://doi.org/10.1126/sciadv.add6439.
160. Gangidine, A.; Havig, J.; Czaja, A. Elemental relics: A trace element biosignature for life on early Earth and Mars. In Proceedings of the Lunar and Planetary Science Conference, The Woodlands, TX, USA, 16–20 March 2020; p. 2520.

161. .Malaterre, C.; Ten Kate, I.L.; Baqué, M.; et al. Is There Such a Thing as a Biosignature? *Astrobiology* **2023**, *23*, 1213–1227. https://doi.org/10.1089/ast.2023.0042.
162. Tait, A.W.; Wilson, S.; Tomkins, A.G.; et al. Evaluation of meteorites as habitats for terrestrial microorganisms: Results from the Nullarbor Plain, Australia, a Mars analogue site. *Geochim. Cosmochim. Acta* **2017**, *215*, 1–16. https://doi.org/10.1016/j.gca.2017.07.025.
163. Cockell, C.S. Trajectories of Martian Habitability. *Astrobiology* **2014**, *14*, 182–203. https://doi.org/10.1089/ast.2013.1106.
164. Westall, F.; Loizeau, D.; Foucher, F.; et al. Habitability on Mars from a Microbial Point of View. *Astrobiology* **2013**, *13*, 887–897. https://doi.org/10.1089/ast.2013.1000.
165. Parker, T.J.; Saunders, R.S.; Schneeberger, D.M. Transitional morphology in West Deuteronilus Mensae, Mars: Implications for modification of the lowland/upland boundary. *Icarus* **1989**, *82*, 111–145. https://doi.org/10.1016/0019-1035(89)90027-4.
166. Grotzinger, J.P.; Gupta, S.; Malin, M.C.; et al. Deposition, exhumation, and paleoclimate of an ancient lake deposit, Gale crater, Mars. *Science* **2015**, *350*, aac7575. https://doi.org/10.1126/science.aac7575.
167. Catling, D.; Wood, S.; Leovy, C.; et al. Light-toned layered deposits in Juventae Chasma, Mars. *Icarus* **2006**, *181*, 26–51. https://doi.org/10.1016/j.icarus.2005.10.020.
168. Watters, T.R.; Campbell, B.; Carter, L.; et al. Radar Sounding of the Medusae Fossae Formation Mars: Equatorial Ice or Dry, Low-Density Deposits? *Science* **2007**, *318*, 1125–1128. https://doi.org/10.1126/science.1148112.
169. Cabrol, N. The Evolution of Lacustrine Environments on Mars: Is Mars Only Hydrologically Dormant? *Icarus* **2001**, *149*, 291–328. https://doi.org/10.1006/icar.2000.6530.
170. Nazari-Sharabian, M.; Aghababaei, M.; Karakouzian, M.; et al. Water on Mars—A Literature Review. *Galaxies* **2020**, *8*, 40. https://doi.org/10.3390/galaxies8020040.
171. Bibring, J.P.; Langevin, Y.; Mustard, J.F.; et al. Global Mineralogical and Aqueous Mars History Derived from OMEGA/Mars Express Data. *Science* **2006**, *312*, 400–404. https://doi.org/10.1126/science.1122659.
172. Milliken, R.E.; Grotzinger, J.P.; Thomson, B.J. Paleoclimate of Mars as captured by the stratigraphic record in Gale Crater. *Geophys. Res. Lett.* **2010**, *37*, L04201. https://doi.org/10.1029/2009gl041870.
173. Duxbury, N.S. Estimating the Past Martian Ocean Depth. *Eur. Geophys. Soc. Tech. Abstr.* **2000**, *22*, 144–146.
174. Brough, S.; Hubbard, B.; Hubbard, A. Area and volume of mid-latitude glacier-like forms on Mars. *Earth Planet. Sci. Lett.* **2019**, *507*, 10–20. https://doi.org/10.1016/j.epsl.2018.11.031.
175. Wang, A.; Kuebler, K.; Jolliff, B.; et al. Mineralogy of a Martian meteorite as determined by Raman spectroscopy. *J. Raman Spectrosc.* **2004**, *35*, 504–514. https://doi.org/10.1002/jrs.1175.
176. Filiberto, J.; Baratoux, D.; Beaty, D.; et al. A review of volatiles in the Martian interior. *Meteorit. Planet. Sci.* **2016**, *51*, 1935–1958. https://doi.org/10.1111/maps.12680.
177. Jakosky, B.M.; Edwards, C.S. Inventory of CO_2 available for terraforming Mars. *Nat. Astron.* **2018**, *2*, 634–639. https://doi.org/10.1038/s41550-018-0529-6.
178. Wade, J.; Dyck, B.; Palin, R.M.; et al. The divergent fates of primitive hydrospheric water on Earth and Mars. *Nature* **2017**, *552*, 391–394. https://doi.org/10.1038/nature25031.
179. Smith, I.B.; Hayne, P.O.; Byrne, S.; et al. The Holy Grail: A road map for unlocking the climate record stored within Mars' polar layered deposits. *Planet. Space Sci.* **2020**, *184*, 104841. https://doi.org/10.1016/j.pss.2020.104841.
180. Hamran, S.E.; Paige, D.A.; Amundsen, H.E.F.; et al. Ground-penetrating radar observations of subsurface structures in Jezero Crater, Mars. *Science* **2022**, *377*, 1325–1329.
181. Zheng, N.; Ding, C.; Su, Y.; et al. Water Ice Resources on the Shallow Subsurface of Mars: Indications to Rover-Mounted Radar Observation. *Remote Sens.* **2024**, *16*, 824. https://doi.org/10.3390/rs16050824.
182. Petrovych, V. Comparison of "ancient" and modern hydrology of Mars. In Proceedings of the VIII International Scientific and Practical Conference: Scientific Advances and Innovative Approaches, Tokyo, Japan, 11–12 January 2024; pp. 9–14.
183. Changela, H.G.; Chatzitheodoridis, E.; Antunes, A.; et al. Mars: New insights and unresolved questions. *Int. J. Astrobiol.* **2021**, *20*, 394–426. https://doi.org/10.1017/s1473550421000276. Correction in *Int. J. Astrobiol.* **2022**, *21*, 46.
184. Clifford, S.M.; Yoshikawa, K.; Byrne, S.; et al. Introduction to the fifth Mars Polar Science special issue: Key questions, needed observations, and recommended investigations. *Icarus* **2013**, *225*, 864–868. https://doi.org/10.1016/j.icarus.2013.04.005.
185. Becerra, P.; Bramson, A.; Brown, A.; et al. The Importance of the Climate Record in the Martian Polar Layered Deposits. *Bull. Am. Astron. Soc.* **2021**, *53*, 144. https://doi.org/10.3847/25c2cfeb.90c37f59.
186. Vos, E.; Aharonson, O.; Schörghofer, N.; et al. Stratigraphic and isotopic evolution of the Martian polar caps from paleo-climate models. *J. Geophys. Res. Planets* **2022**, *127*, e2021JE007115. https://doi.org/10.1029/2021JE007115.
187. ISRO. Payloads (Mars Orbiter Mission Payload Datasets. Indian Space Research Organisation). 2023. Available online at https://www.isro.gov.in/mission_payloads.html (accessed on 23 September 2026).
188. Levrard, B.; Forget, F.; Montmessin, F.; et al. Recent formation and evolution of northern Martian polar layered deposits as inferred from a Global Climate Model. *J. Geophys. Res. Planets* **2007**, *112*, E06012. https://doi.org/10.1029/2006je002772.

189. Bierson, C.J.; Tulaczyk, S.; Courville, S.W.; et al. Strong MARSIS Radar Reflections from the Base of Martian South Polar Cap May Be Due to Conductive Ice or Minerals. *Geophys. Res. Lett.* **2021**, *48*, e2021GL093880. https://doi.org/10.1029/2021gl093880.
190. Zhou, J.; Ding, C.; Xiong, S.; et al. Radar Observations of Liquid Water in the South Polar Region of Mars: Indications from Astrobiology Perspectives. *Universe* **2024**, *10*, 43. https://doi.org/10.3390/universe10010043.
191. Singh, R.; Chauhan, P. Observations of North Polar Region of Mars from the Mars Colour Camera Onboard Indian Mars Orbiter Mission. *J. Indian Soc. Remote Sens.* **2023**, *51*, 1825–1840. https://doi.org/10.1007/s12524-023-01745-6.
192. Ball, E.R.; Seviour, W.J.M.; Mitchell, D.M. The Importance of Isentropic Mixing in the Formation of the Martian Polar Layered Deposits. *Planet. Sci. J.* **2023**, *4*, 213. https://doi.org/10.3847/psj/ad045d.
193. Wu, Z.; Li, T.; Heavens, N.G.; et al. Earth-like thermal and dynamical coupling processes in the Martian climate system. *Earth-Sci. Rev.* **2022**, *229*. 104023. https://doi.org/10.1016/j.earscirev.2022.104023.
194. Vlasov, P.V.; Ignatiev, N.I.; Korablev, O.I.; et al. Thermal Sounding of the Martian Atmosphere Using the ACS TIRVIM FT-IR Spectrometer on Board ExoMars TGO: Method for Solving the Inverse Problem. *Sol. Syst. Res.* **2023**, *57*, 516–532. https://doi.org/10.1134/s0038094623060084.
195. Nagle-McNaughton, T.P.; Scuderi, L.A.; Erickson, N. Squeezing Data from a Rock: Machine Learning for Martian Science. *Geosciences* **2022**, *12*, 248. https://doi.org/10.3390/geosciences12060248.
196. Moores, J.E.; Smith, P.H.; Tanner, R. The effect of martian surface geometry on ultraviolet fluxes. In Proceedings of the 37th Annual Lunar and Planetary Science Conference, League City, TX, USA, 13–17 March 2006; p. 2340.
197. Schuerger, A.C.; Mickol, R.L.; Schwendner, P. The Hypopiezotolerant Bacterium, Serratia liquefaciens, Failed to Grow in Mars Analog Soils under Simulated Martian Conditions at 7 hPa. *Life* **2020**, *10*, 77. https://doi.org/10.3390/life10060077.
198. Zhou, W.Y.; Olson, P.L.; Shearer, C.K.; et al. High pressure-temperature phase equilibrium studies on Martian basalts: Implications for the failure of plate tectonics on Mars. *Earth Planet. Sci. Lett.* **2022**, *594*, 117751. https://doi.org/10.1016/j.epsl.2022.117751.
199. Çelekli, A.; Zariç, Ö.E. Breathing life into Mars: Terraforming and the pivotal role of algae in atmospheric genesis. *Life Sci. Space Res.* **2024**, *41*, 181–190. https://doi.org/10.1016/j.lssr.2024.03.001.
200. Moresi, L.; Solomatov, V. Mantle convection with a brittle lithosphere: Thoughts on the global tectonic styles of the Earth and Venus. *Geophys. J. Int.* **1998**, *133*, 669–682. https://doi.org/10.1046/j.1365-246x.1998.00521.x.
201. Lourenço, D.L.; Rozel, A.B.; Ballmer, M.D.; et al. Plutonic-Squishy Lid: A New Global Tectonic Regime Generated by Intrusive Magmatism on Earth-Like Planets. *Geochem. Geophys. Geosyst.* **2020**, *21*, e2019GC008756. https://doi.org/10.1029/2019gc008756.
202. Rolf, T.; Weller, M.; Gülcher, A.; et al. Dynamics and Evolution of Venus' Mantle through Time. *Space Sci. Rev.* **2022**, *218*, 70. https://doi.org/10.1007/s11214-022-00937-9.
203. Solomatov, V.S.; Moresi, L.N. Stagnant lid convection on Venus. *J. Geophys. Res. Planets* **1996**, *101*, 4737–4753. https://doi.org/10.1029/95je03361.
204. Yung, Y.L.; Nair, H.; Gerstell, M.F. CO_2 Greenhouse in the Early Martian Atmosphere: SO_2 Inhibits Condensation. *Icarus* **1997**, *130*, 222–224. https://doi.org/10.1006/icar.1997.5808.
205. McKay, C.P.; Marinova, M.M. The Physics, Biology, and Environmental Ethics of Making Mars Habitable. *Astrobiology* **2001**, *1*, 89–109. https://doi.org/10.1089/153110701750137477.
206. Salazar, F.J.T.; Winter, O.C. Sun-synchronous solar reflector orbits designed to warm Mars. *Astrophys. Space Sci.* **2019**, *364*, 147. https://doi.org/10.1007/s10509-019-3633-x.
207. Brain, D.A.; Bagenal, F.; Ma, Y.-J.; et al. Atmospheric escape from unmagnetized bodies. *J. Geophys. Res. Planets* **2016**, *121*, 2364–2385. https://doi.org/10.1002/2016JE005162.
208. Bamford, R.A.; Kellett, B.J.; Green, J.L.; et al. How to create an artificial magnetosphere for Mars. *Acta Astronaut.* **2022**, *190*, 323–333. https://doi.org/10.1016/j.actaastro.2021.09.023.
209. Peroni, D. Microbial life as a tool for ecological engineering and future Martian biospheres. *Astrobiology* **2018**, *18*, 210–222.
210. Schwendner, P.; Schuerger, A.C. Survival and metabolic kinetics of Nostoc commune under simulated Martian surface conditions. *Astrobiology* **2020**, *20*, 485–499.
211. Nanda, R.; Ankur, R.; Chundri, R.; et al. Microbial colonization of mars. In Proceedings of the 73rd International Astronautical Congress (IAC), Paris, France, 18–22 September 2022.
212. Gómez, F.; Rodríguez-Manfredi, J.A.; Rodríguez, N.; et al. Habitability: Where to look for life? Halophilic habitats: Earth analogs to study Mars habitability. *Planet. Space Sci.* **2012**, *68*, 48–55. https://doi.org/10.1016/j.pss.2011.12.021.
213. Mukhin, L.M. Volcanic processes and synthesis of simple organic compounds on primitive Earth. *Orig. Life* **1976**, *7*, 355–368. https://doi.org/10.1007/bf00927931.